Czech Technical University
in Prague

Faculty of Nuclear Sciences and Physical
Engineering

Department of Physics

MASTER'S THESIS

Calculations of antibaryon bound states in atomic nuclei

Jaroslava Hrtánková

2013

Supervisor: RNDr. Jiří Mareš, CSc.

České vysoké učení technické
v Praze

Fakulta jaderná a fyzikálně inženýrská

Katedra fyziky

DIPLOMOVÁ PRÁCA

Výpočty viazaných stavov antibaryónov v atómových jadrách

Jaroslava Hrtánková

2013

Školiteľ: RNDr. Jiří Mareš, CSc.

Prehlásenie

Prehlasujem, že som svoju diplomovú prácu vypracovala samostatne a použila som iba podklady (literatúru, projekty, SW atd.) uvedené v priloženom zozname.

Nemám závažný dôvod proti použitiu tohto školského diela v zmysle zákona §60 Zákona č.121/2000 Sb., o práve autorskom, o právach súvisiacich s právom autorským a o zmene niektorých zákonov (autorský zákon).

Declaration

I declare that I wrote my Master's thesis independently and exclusively within the use of cited bibliography.

I agree with the usage of this thesis in the purport of the Act 121/2000 (Copyright Act).

V Prahe dňa ....

Jaroslava Hrtánková

Acknowledgement

I would like to thank my supervisor, Dr. Jiří Mareš, for his professional assistance and useful discussions throughout writing this work.

Thesis tittle:	**Calculations of antibaryon bound states in atomic nuclei**
Author:	Jaroslava Hrtánková
Department:	Department of Physics FNSPE CTU in Prague
Branch of study:	Nuclear Engineering
Kind of thesis:	Master's thesis
Supervisor:	RNDr. Jiří Mareš, CSc.

Abstract: This thesis deals with the interaction of antibaryons with the nuclear medium. We calculated $\bar{p}$, $\bar{\Lambda}$, $\bar{\Sigma}$ and $\bar{\Xi}$ bound states in selected nuclei within the relativistic mean-field (RMF) model, employing the G-parity motivated antibaryon–meson coupling constants. Possible deviations from the G-parity were taken into account by introducing a scaling factor. The self-consistent dynamical calculations using various RMF parametrizations revealed huge polarization effects inside a nucleus due to the presence of an antibaryon. The central density reaches about 3 times the normal nuclear density. The antibaryons feel strong attractive potential and are thus deeply bound in nuclei. We incorporated the $\bar{p}$ absorption in the nuclear medium by including the phenomenological imaginary part of the optical potential which was constrained by fits to $\bar{p}$-atomic data. We took into account the reduction of the phase space available for the annihilation products which led to a significant suppression of the $\bar{p}$ absorption widths.

Keywords: antibaryon–nucleus interaction, RMF model, G-parity, nuclear density, binding energy, annihilation

Názov práce: **Výpočty viazaných stavov antibaryónov v atómových jadrách**

Autor: Jaroslava Hrtánková

Katedra: Katedra fyziky FJFI ČVUT v Prahe

Obor štúdia: Jadrové inžinierstvo

Druh práce: Diplomová práca

Školiteľ: RNDr. Jiří Mareš, CSc.

Abstrakt: V tejto diplomovej práci sa zaoberáme skúmaním interakcie antibaryónov s atómovými jadrami. Uskutočnili sme výpočty viazaných stavov $\bar{p}$, $\bar{\Lambda}$, $\bar{\Sigma}$ a $\bar{\Xi}$ vo vybraných atómových jadrách v rámci relativistickej teórie stredných polí (RMF), pri výpočtoch sme použili antibaryón–mezónové väzbové konštanty získané pomocou G-parity. Možné odchlýky od presnej G-parity sme zobrali do úvahy zavedením škálovacieho parametra. Selfkonzistentné dynamické výpočty odhalili silné polarizačné efekty v jadre spôsobené prítomnosťou antibaryónu. Centrálna hustota v jadre vzrástla asi trojnásobne oproti normálu. Zistili sme, že antibaryóny cítia v jadre silné priťahovanie a sú následne hlboko viazané. Vo výpočtoch sme uvažovali absorpciu $\bar{p}$ v jadre, ktorú sme realizovali pridaním imaginárnej časti fenomenologického optického potenciálu. Jeho parametre boli určené z fitov na $\bar{p}$-atómové dáta. Ďalej sme uvažovali aj redukciu fázového priestoru pre produkty anihilácie, čo viedlo k dramatickému poklesu antiprotónových šírok.

Kľúčové slová: antibaryón–jadrová interakcia, RMF model, G-parita, jadrová hustota, väzbová energia, anihilácia

Contents

Chapter 1

Introduction

The study of interactions of antibaryons with a nucleus is a source of valuable information about the behavior of the antibaryon ($\bar{B}$) in nuclear matter, the in-medium $\bar{B}N$ interaction and nuclear dynamics. It may serve as a test of models of baryon–baryon interaction as well as of various nuclear models.

The possibility of the existence of antibaryon–nucleus bound states has attracted considerable interest in recent years. Numerous articles has been written on this topic [1, 2, 3, 4, 5]. Much attention has been devoted to the antiproton–nucleus interaction and the possibility of producing the $\bar{p}$–nucleus bound states at future experimental facilities [1, 6]. However, the experimental information about the $\bar{p}$–nucleus interaction is still rather limited.

The experiments aiming at exploring the $\bar{p}$–nucleon interaction has been performed since the discovery of the antiproton in 1955 [7]. In the 1960's, the $\bar{p}$ annihilation was studied by stopping antiprotons in a bubble chamber in experiments at the Brookhaven National Laboratory (BNL) and CERN [8]. Later, reactions with $\bar{p}$ were explored at the LEAR facility, CERN [9]. The $\bar{p}$ elastic and inelastic scattering off nuclei and proton knock-out reactions were analyzed in order to get more information about the $\bar{p}$–nucleus potential. The measurements of the differential cross-section for the $\bar{p}$ elastic scattering off ^{12}C at 46.8 MeV at LEAR revealed a deep absorptive and a shallow attractive part of the $\bar{p}$–nucleus potential [10]. The Crystal Barrel Collaboration studied annihilation channels as a function of the $\bar{p}$ momentum [11]. The $\bar{p}$ interaction with protons and nuclei at rest and very low momenta was investigated in the Obelix experiment (see [12] and references therein).

Valuable information about the $\bar{p}$–nucleus optical potential has been provided by antiprotonic atoms [13, 14]. An antiprotonic atom is a sort of an exotic atom which is created whenever an electron in atomic orbit is replaced by a negatively charged hadron. As the (anti)hadron (e.g. $\bar{p}, \pi^-, \Sigma^-, K^-$) is much heavier than the electron it gets considerably closer to the nucleus. Consequently, it interacts with the nucleus

not only electromagnetically but also by strong interaction. The strong interaction causes energy shifts (ϵ) and widths (Γ) of atomic levels, which are measured by experiment. The strong interaction shifts and widths can be calculated by adding an optical potential into the relevant equation of motion. The imaginary part of this potential describes absorption of the (anti)hadron in the nuclear medium.

The optical potential in a '$t\rho$' form was used to fit 107 data points of X-ray and radiochemical data [15]. Various shapes of the nuclear density distribution were used in those fits. Unfortunately, the optical potential could be determined at radii where the nuclear density reaches just a few per cent of the central nuclear density. The global fits led to the potential with the attractive real part about 110 MeV deep and the absorptive imaginary part about 160 MeV deep when extrapolated into the nuclear interior [15].

The results of the above analyses indicate that $\bar{p}$ would not penetrate into the nuclear interior because it annihilates at the surface region due to the strong absorption in the nuclear medium. No evidence for $\bar{p}$–nucleus bound state has been obtained so far [16].

The theoretical predictions of antiproton–nucleus bound states are based on the symmetry between the NN and $\bar{N}N$ potential. The NN and $\bar{N}N$ potentials are related to each other by the G-parity transformation. In the framework of the meson exchange theory, the $\bar{N}N$ potential inspired by the G-parity transformation is strongly attractive and has no repulsive core [17]. This suggests that the antiproton should be bound deeply in the nucleus. Similar predictions based on the G-parity transformation can be made about the potentials for $\bar{\Lambda}, \bar{\Sigma}, \bar{\Xi}$ antihyperons.

In recent years, frequently used approaches to the study of nuclear structure are based on relativistic models which describe a nucleus as a system of strongly interacting nucleons and mesons. These models are formulated in the framework of the relativistic quantum field theory. Relativistic models of a nucleus have become quite popular because they naturally incorporate the spin-orbit force and account for nuclear matter saturation. The prototype of such an approach is the relativistic mean-field model (RMF) [18, 19]. The RMF model proved to be efficient tool for calculating various properties of finite nuclei, such as binding energies, root mean square (RMS) radii and single particle spectra [20].

Antiproton bound states in ^{16}O and ^{208}Pb were calculated within the RMF model using G-parity motivated $\bar{p}$ coupling constants by Bürvenich et al. [1]. The self-consistent calculations, taking into account the rearrangement of the nuclear core, led to a strong binding of the antiproton inside a nucleus. They also revealed large compression of the nucleus induced by the presence of the $\bar{p}$. The central density reached values about $2-4$ times the normal nuclear density.

The annihilation of the $\bar{p}$ in the nuclear medium was studied as well. It may seem that the $\bar{p}$ has to annihilate immediately in the nucleus and, therefore, it can not live long enough to create an observable bound state. However, the phase space available for annihilation products can be considerably suppressed for the antiproton deeply bound in a nucleus. Consequently, many annihilation channels are simply closed in the medium. Taking into account the phase space suppression, the life time of the bound antiproton–nucleus system has been estimated to $2 - 20$ fm in Ref. [1].

In Ref. [2], the dynamical transport model [21] was used to calculate the time needed for the formation of a compressed $\bar{p}$–nucleus system. The calculations revealed that, after the creation of the initial state, it takes about $4 - 10$ fm to reach the maximal central density of order $2 - 3\rho_0$ (where $\rho_0 = 0.16$ fm^{-3}) in a $\bar{p}$-nucleus system. They have also demonstrated, that the $\bar{p}$ annihilation in the nucleus could lead to the multifragmentation of the nucleus. This might serve as an observable signature for the antiproton–nucleus bound state.

Hyperons and antihyperons are interesting particles with non-zero strangeness. A hyperon represents a suitable probe for studying the nuclear structure as it is not restricted by the Pauli principle in the nuclear medium. A nucleus containing one or more hyperons is called a hypernucleus. Hypernuclei are widely explored systems in many experiments [22, 23]. They provide valuable information about baryon–baryon interactions in the nuclear medium, nuclear structure, as well as weak interaction [24].

Antihyperon–nucleus bound states were studied in Ref. [1], where the calculations of $\bar{\Lambda}$ embedded in several nuclei were performed. The $\bar{\Lambda}$ was found to be deeply bound in the nucleus and its presence caused sizeable compression of the nuclear core. The same effect could be expected also in nuclei containing other antihyperons. The question of the antihyperon annihilation in the nuclear medium was examined as well [1]. It is assumed that the $\bar{\Lambda}$ could live quite long in a nucleus. The suppression of the phase space available for the annihilation products should be more pronounced than in the case of the antiproton. It is due to the presence of a heavy kaon in the lowest mass annihilation channel.

New experiments with highly energetic antiprotons of $1 - 15$ GeV are planned at the FAIR facility (Darmstadt). One of its parts, the PANDA experiment [6], is going to explore the interaction of antiprotons with nucleons and nuclei in order to study the hadron structure. These measurements are expected to provide us with new information about the $\bar{p}$N potential and $\bar{p}$ annihilation in the nuclear medium. Moreover, the information about the antihyperon–nucleon potential may be obtained in the antiproton–nucleus reaction via the production of antihyperon–

hyperon pairs after the antiproton–proton annihilation [25].

In this thesis, the interaction of selected antibaryons, namely $\bar{p}, \bar{\Lambda}, \bar{\Sigma}$ and $\bar{\Xi}$, with nuclei is studied. We performed detailed calculations of various nuclear systems throughout the periodic table within several RMF models, taking into account dynamical effects due to the strongly interacting antibaryon. While considering the annihilation of the antiproton in the nuclear medium we took into account the reduction of the phase space available for the decay products of the deeply bound $\bar{p}$. In the second chapter, the RMF model is introduced and the equations of motion for a nucleus with an antibaryon are derived. The results of self-consistent calculations of antibaryon bound states in selected nuclei are discussed in Chapter 3. Conclusions are summarized in Chapter 4. The notation used in this work is briefly introduced in Appendix A, while the details of numerical calculations are presented in Appendix B.

Chapter 2

Relativistic mean-field approach

In this work, the interaction of antibaryons with nuclei is described in the framework of the RMF model [18, 19]. In this model, (anti)baryons are treated as Dirac fields ψ interacting via the exchange of meson fields. The meson fields are sorted by their internal angular momentum J, parity P, isospin T and only fields with natural parity are employed. The formalism incorporates the following fields: isoscalar-scalar field σ responsible for the medium range attraction between nucleons, isoscalar-vector field ω_μ which mediates the short range repulsion, isovector-vector field $\vec{\rho}_\mu$ which allows to adjust isovector properties of nuclei, and massless vector field A_μ which mediates the electromagnetic interaction. The RMF model is based on two approximations: the *mean-field* approximation and the *no-sea* approximation, which allow us to solve the equations of motion.

2.1 Model Lagrangian density

The starting point of the RMF model is the effective Lagrangian density for a system of nucleons interacting via the exchange of aforementioned meson fields:

$$\begin{aligned}\mathscr{L} =& \hat{\bar{\psi}}[i\gamma^\mu\partial_\mu - m_N - g_\sigma\hat{\sigma} - g_\omega\gamma_\mu\hat{\omega}^\mu - g_\rho\gamma_\mu\vec{\tau}\cdot\hat{\vec{\rho}}^\mu - e\gamma_\mu\frac{1}{2}(1+\tau_3)\hat{A}^\mu]\hat{\psi} \\ &+ \frac{1}{2}\left(\partial_\mu\hat{\sigma}\partial^\mu\hat{\sigma} - m_\sigma^2\hat{\sigma}^2\right) - \frac{1}{2}(\frac{1}{2}\hat{\Omega}_{\mu\nu}\hat{\Omega}^{\mu\nu} - m_\omega^2\hat{\omega}^\mu\hat{\omega}_\mu) \\ &- \frac{1}{2}(\frac{1}{2}\hat{\vec{R}}_{\mu\nu}\cdot\hat{\vec{R}}^{\mu\nu} - m_\rho^2\hat{\vec{\rho}}_\mu\cdot\hat{\vec{\rho}}^\mu) - \frac{1}{4}\hat{F}_{\mu\nu}\hat{F}^{\mu\nu} \\ &- \frac{1}{3}g_2\hat{\sigma}^3 - \frac{1}{4}g_3\hat{\sigma}^4 + \frac{1}{4}d(\hat{\omega}^\mu\hat{\omega}_\mu)^2 \ ,\end{aligned} \tag{2.1}$$

where the arrow denotes an isovector quantity and $\vec{\tau}$ is the triplet of Pauli matrices; m_N denotes the mass of the nucleon; m_σ, m_ω, m_ρ are the masses of the σ-, ω- and ρ-meson; $g_{\sigma N}$, $g_{\omega N}$, $g_{\rho N}$ and e are the coupling constants of the corresponding fields

with nucleons. The g_2, g_3 and d represent the strengths of the scalar σ and vector ω field self-interaction. All considered fields in the above Lagrangian density are treated as quantum fields. The field tensors $\hat{G}_{\mu\nu}$ ($\hat{G} = \hat{\Omega}, \hat{F}$) and $\hat{\vec{R}}_{\mu\nu}$ of the vector fields are defined as:

$$\begin{aligned} \hat{G}_{\mu\nu} &= \partial_\mu \hat{G}_\nu - \partial_\nu \hat{G}_\mu \ , \\ \hat{\vec{R}}_{\mu\nu} &= \partial_\mu \hat{\vec{\rho}}_\nu - \partial_\nu \hat{\vec{\rho}}_\mu - g_{\rho N}(\hat{\vec{\rho}}_\mu \times \hat{\vec{\rho}}_\nu) \ . \end{aligned} \tag{2.2}$$

2.2 Model approximations

In order to simplify the handling with quantum fields, the *mean-field* approximation is applied. It means that all quantum fluctuations of the meson fields are omitted and the fields are treated as classical ones. Practically, we replace all meson quantum fields with their expectation values, e. g.:

$$\hat{\sigma} \to \sigma = \langle \sigma \rangle \ , \tag{2.3}$$

and similarly for the other fields. The nucleons then behave like independent particles moving in the meson mean fields.

The *no-sea* approximation consists in omitting the contribution from vacuum polarization. It means that we neglect the contribution of antiparticles and take into account only the contribution of A nucleons in the nucleus. The nucleon field operator can be expanded in terms of the single particle states α as

$$\hat{\psi} = \sum_\alpha \psi^\alpha(x^\mu)\hat{a}_\alpha \ , \tag{2.4}$$

where $\hat{a}_\alpha$ is the annihilation operator for a nucleon in the state α and $\psi^\alpha(x^\mu)$ is the single particle wave function. The densities reduce then to sums over the single particle states, e. g. the scalar density

$$\hat{\bar{\psi}}\hat{\psi} = \sum_{\alpha=1}^{A} \bar{\psi}^\alpha \psi^\alpha \ , \tag{2.5}$$

where the sum runs over the A nucleons bound in a nucleus.

Furthermore, we are interested in stationary states and spherically symmetric nuclei. The stationarity implies that all time derivatives of the fields will vanish. Rotational invariance implies that all spatial components of the fields will be zero

as well

$$\dot{\sigma} = 0, \quad \dot{\omega}_\mu = 0, \quad \dot{\vec{\rho}}_\mu = 0, \quad \dot{A}_\mu = 0 \ , \tag{2.6}$$

$$\langle \omega_i \rangle = 0, \quad \langle \vec{\rho}_i \rangle = 0, \quad \langle A_i \rangle = 0 \quad \text{for } i\text{=1,2,3} \ . \tag{2.7}$$

We assume that single particle states do not mix isospin, i. e., only the neutral component of the isovector ρ-meson field is considered. After the above assumptions, only the σ, ω_0, ρ_0 and A_0 fields remain. The time dependence of the (anti)baryon wave function is as follows

$$\psi^\alpha(x) = e^{-i\epsilon^\alpha t}\psi^\alpha(\vec{x}) \ , \tag{2.8}$$

where ϵ^α are the single particle energies.

2.3 RMF model for a nucleus with an antibaryon

When we adopt the above approximations, the Lagrangian density (2.1) for a system of nucleons and antibaryons will acquire the form

$$\begin{aligned}\mathscr{L}_{\rm RMF} = \sum_{j=N,\bar{B}} \bar{\psi}_j^\alpha (i\gamma_\mu \partial^\mu - m_j - g_{\sigma j}\sigma - g_{\omega j}\gamma_0\omega_0 - g_{\rho j}\gamma_0\tau_3\rho_0 - e\gamma_0\frac{1+\tau_3}{2}A_0)\psi_j^\alpha \\ - \frac{1}{3}g_2\sigma^3 - \frac{1}{4}g_3\sigma^4 + \frac{1}{4}d\omega_0^4 - \frac{1}{2}[(\nabla_i\sigma)^2 + m_\sigma^2\sigma^2] \\ + \frac{1}{2}[(\nabla_i\omega_0)^2 + m_\omega^2\omega_0^2] + \frac{1}{2}[(\nabla_i\rho_0)^2 + m_\rho^2\rho_0^2] + \frac{1}{2}(\nabla_i A_0)^2 \ .\end{aligned} \tag{2.9}$$

Using the Hamilton's variational principle with respect to given fields $\psi_j, \sigma, \omega_0, \rho_0$, and A_0, we derive the equations of motion for a system of interacting nucleons and antibaryons. The Dirac equation for the nucleons and antibaryons is as follows

$$[-i\vec{\alpha}\vec{\nabla} + \beta(m_j + S_j) + V_j]\psi_j^\alpha = \epsilon_j^\alpha \psi_j^\alpha, \quad j = N, \bar{B} \ , \tag{2.10}$$

where

$$S_j = g_{\sigma j}\sigma, \quad V_j = g_{\omega j}\omega_0 + g_{\rho j}\rho_0\tau_3 + e_j\frac{1+\tau_3}{2}A_0 \ .$$

The Klein–Gordon equations for meson fields read

$$\begin{aligned}
(-\triangle + m_\sigma^2 + g_2\sigma + g_3\sigma^2)\sigma &= -\sum_j g_{\sigma j}\rho_{\mathrm{S}j} \ , \\
(-\triangle + m_\omega^2 + d\omega_0^2)\omega_0 &= \sum_j g_{\omega j}\rho_{\mathrm{V}j} \ , \\
(-\triangle + m_\rho^2)\rho_0 &= \sum_j g_{\rho j}\rho_{\mathrm{I}j} \ , \\
-\triangle A_0 &= \sum_j e_j\rho_{\mathrm{Q}j} \ ,
\end{aligned} \tag{2.11}$$

where $\rho_{\mathrm{S}j}, \rho_{\mathrm{V}j}, \rho_{\mathrm{I}j}$ and $\rho_{\mathrm{Q}j}$ are the scalar, vector, isovector and charge densities, respectively, defined as

$$\begin{aligned}
\rho_{\mathrm{S}j} &= \sum_\alpha \bar{\psi}_j^\alpha \psi_j^\alpha \ , \\
\rho_{\mathrm{V}j} &= \sum_\alpha \bar{\psi}_j^\alpha \beta \psi_j^\alpha \ , \\
\rho_{\mathrm{I}j} &= \sum_\alpha \bar{\psi}_j^\alpha \beta \tau_3 \psi_j^\alpha \ , \\
\rho_{\mathrm{Q}j} &= \sum_\alpha \bar{\psi}_j^\alpha \beta \frac{1+\tau_3}{2} \psi_j^\alpha \ ,
\end{aligned} \tag{2.12}$$

where the sums run over all occupied single-particle states α. The system of Dirac and Klein–Gordon equations (2.10) and (2.11) represent a self-consistent problem which is to be solved by iterative procedure. At the beginning, we start from a reasonable estimate of the meson and electromagnetic fields and solve the Dirac equation. It yields the nucleon and antibaryon wave functions which are used to evaluate the densities (2.12). Then, the densities are used as a new source terms in the Klein–Gordon equations (2.11) to calculate new meson and electromagnetic fields. These are again inserted into the Dirac equation which yields nucleon and antibaryon spinors for the next iteration. This procedure is repeated until the self-consistency is reached. A detailed numerical solution is given in Appendix B.

After we obtain the solution for nucleon, antibaryon and meson fields we can calculate physical quantities characterizing the system, such as the total binding energy, (anti)baryon separation energy, density distributions, and root mean square

(RMS) radii. The total binding energy for the system of nucleons and antibaryon is

$$\begin{aligned} -B &= E + E_{\rm CMS} - A m_N - m_{\bar{B}} \\ &= \textstyle\sum_\alpha (\epsilon_N^\alpha - m_N) + (\epsilon_{\bar{B}}^\alpha - m_{\bar{B}}) \\ &- \frac{1}{2}\int {\rm d}^3x \, (-g_{\sigma N}\, \sigma \rho_{\rm SN} + g_{\omega N}\, \omega_0 \rho_{\rm VN} + g_{\rho N}\, \rho_0 \rho_{\rm IN} + e\, A_0 \rho_{\rm QN}) \\ &- \frac{1}{2}\int {\rm d}^3x \, (-\tfrac{1}{3} g_2\, \sigma^3 - \tfrac{1}{2} g_3\, \sigma^4 + \tfrac{1}{2} d\, \omega^4) \\ &- \frac{1}{2}\int {\rm d}^3x \, (-g_{\sigma \bar{B}}\, \sigma \rho_{S\bar{B}} + g_{\omega \overline{B}}\, \omega_0 \rho_{V\bar{B}} + g_{\rho \bar{B}}\, \rho_0 \rho_{I\bar{B}} - e\, A_0 \rho_{\bar{B}}) \\ &- 30.75\ (A+1)^{-1/3} [{\rm MeV}] \ , \end{aligned} \tag{2.13}$$

where $E_{\rm CMS}$ is the center-of-mass energy, ϵ_j^α is the single particle energy of the (anti)baryon. The RMS radius is defined as

$$r_{\rm RMS} = \sqrt{\int_V r^2 \bar{\psi}^\alpha \psi^\alpha dV} \ . \tag{2.14}$$

2.4 Density–dependent RMF model

When investigating the interaction of an antibaryon with a nucleus we found strong polarization of the nuclear core. The presence of the antibaryon in the nucleus causes massive changes in the nuclear density distribution. The core density reaches $3-4$ times the normal nuclear density. The models with constant couplings do not necessarily describe correctly the behavior of the nucleus when extrapolated to such high densities. A density dependence of coupling constants was introduced in order to improve the equation of state of nuclear matter at higher densities. The parameters of the density–dependent model are fitted in such a way that the model describes well not only the properties of finite nuclei and nuclear matter in the vicinity of saturation point but also at higher densities.

In the density–dependent RMF model proposed by Typel and Wolter [26], the meson–nucleon coupling constants $g_{\sigma N}, g_{\omega N}$ and $g_{\rho N}$ become a function of the vector density $\rho_{\rm VN}$. The dependence of $g_{\sigma N}, g_{\omega N}$ on the baryon density is of the form

$$g_{iN}(\rho_{\rm VN}) = g_{iN}(\rho_0) f_i(x) \ , \quad i = \sigma, \omega \ , \tag{2.15}$$

where

$$f_i(x) = a_i \frac{1 + b_i (x + d_i)^2}{1 + c_i (x + d_i)^2} \tag{2.16}$$

is a function of $x = \rho_{\rm VN}/\rho_0$ and ρ_0 denotes the saturation density of nuclear matter.

The coupling for the ρ meson has an exponential character

$$g_{\rho N}(\rho_{VN}) = g_{\rho N}(\rho_0) exp[-a_\rho(x-1)] \ . \tag{2.17}$$

The parameters a_i, b_i, c_i, d_i and a_ρ are obtained from fits to nuclear properties and constrained by conditions on the functions $f_i(x)$. In this model, the meson self interactions are set to zero, i. e. $g_2 = g_3 = d = 0$.

The Lagrangian density for the density–dependent model has formally the same form as (2.1), only the coupling constants now depend on the vector density $\rho_{\mathrm{V}N}$. The density dependence leads to an extra term appearing in the Dirac equation

$$[-i\vec{\alpha}\vec{\nabla} + \beta(m_j + S_j) + V_j]\psi_j^\alpha = \epsilon_j^\alpha \psi_j^\alpha \ , \quad j = N, \bar{B} \ , \tag{2.18}$$

where

$$S_j = g_{\sigma j}\sigma, \quad V_j = g_{\omega j}\omega_0 + g_{\rho j}\rho_0\tau_3 + e_j\frac{1+\tau_3}{2}A_0 + \Sigma_{\mathrm{R}} \ . \tag{2.19}$$

The rearrangement term Σ_{R}, which comes from the density dependence of coupling constants, acquires the form

$$\Sigma_{\mathrm{R}} = \frac{\partial g_{\omega N}}{\partial \rho_{\mathrm{V}N}}\rho_{\mathrm{V}N}\omega_0 + \frac{\partial g_{\rho N}}{\partial \rho_{\mathrm{V}N}}\rho_{\mathrm{I}N}\rho_0 - \frac{\partial g_{\sigma N}}{\partial \rho_{\mathrm{V}N}}\rho_{\mathrm{S}N}\sigma \ . \tag{2.20}$$

The Klein–Gordon equations for meson fields with density–dependent coupling constants will maintain their form as in (2.11). Due to the density dependence (DD) of the couplings, the rearrangement term will appear in the equation for the total binding energy

$$\begin{aligned} -B &= E_{\mathrm{DD}} + E_{\mathrm{CMS}} - Am_N - m_{\bar{B}} \\ &= \textstyle\sum_{\alpha=1}(\epsilon_\alpha - m_N) + (\epsilon_{\bar{B}} - m_{\bar{B}}) \\ &- \frac{1}{2}\int \mathrm{d}^3x \ (-g_{\sigma N}\,\sigma\rho_{\mathrm{S}N} + g_{\omega N}\,\omega_0\rho_{\mathrm{V}N} + g_{\rho N}\,\rho_0\rho_{\mathrm{I}N} + e\,A_0\rho_{\mathrm{Q}N} + 2\Sigma_{\mathrm{R}}) \\ &- \frac{1}{2}\int \mathrm{d}^3x \ (-g_{\sigma\bar{B}}\,\sigma\rho_{\mathrm{S}\bar{B}} + g_{\omega\bar{B}}\,\omega_0\rho_{\mathrm{V}\bar{B}} + g_{\rho\bar{B}}\,\rho_0\rho_{\mathrm{I}\bar{B}} - e\,A_0\rho_{\bar{B}}) \\ &- 30.75\ (A+1)^{-1/3}[\mathrm{MeV}] \ . \end{aligned} \tag{2.21}$$

2.5 Antibaryon–nucleus interaction

When we intend to describe the antibaryon–nucleus interaction within the RMF model, we need to know the strength of the antibaryon–meson coupling. In the framework of the meson exchange theory, the BN and $\bar{B}N$ interactions are related by the G-parity transformation. It involves the charge conjugation and a rotation

in isospin space $\hat{G} = \hat{C}\exp(-i\pi I_2)$. The G-parity is a general rule and reflects the basic symmetries of strong interaction. It links states with the same isospin quantum number and transforms, e. g., a nucleon to an antinucleon

$$\hat{G}\,|N\rangle = |\bar{N}\rangle \ , \tag{2.22}$$

where $|N\rangle$ and $|\bar{N}\rangle$ denotes a nucleon and antinucleon state, respectively [27].

All non-strange mesons are eigenstates of $\hat{G}$ with eigenvalue ± 1, e. g., a system of n pions has eigenvalue $(-1)^n$. The contribution of various mesons to $\bar{B}N$ interaction will then differ from BN interaction by their G-parity eigenvalue. According to this rule, the potential for an antibaryon can be obtained by the transformation of the baryon potential

$$V_{\bar{B}N} = \sum_m G_m V_m \ , \tag{2.23}$$

where m denotes the exchanged meson and G_m denotes the value of the G-parity for the meson field.

In the RMF model, we use the meson fields σ, ω, ρ and photon field γ to describe the nucleon–nucleus interaction. The meson fields σ, ρ and photon field γ have positive G-parity, while the ω field has negative G-parity. In case of the $\bar{p}$–nucleus interactions, the coupling constants for the antiproton will be then in the following relationships to the nucleon coupling constants

$$g_{\sigma\bar{p}} = g_{\sigma N}, \quad g_{\omega\bar{p}} = -g_{\omega N}, \quad g_{\rho\bar{p}} = g_{\rho N} \ . \tag{2.24}$$

The nuclear ground state is well described by an attractive scalar potential $|S| \simeq 350$ MeV and a repulsive vector potential $|V| \simeq 300$ MeV. The resulting total potential for slow nucleons is $S + V \simeq -50$ MeV. However, for the antiproton the vector potential becomes attractive due to the G-parity transformation and, therefore, we obtain really deep central potential $S - V \simeq -650$ MeV. It indicates that the $\bar{p}$ would be bound very strongly in a nucleus. However, the exact G-parity symmetry is an idealization. The fits to $\bar{p}$-atomic data give the real part of the $\bar{p}$ potential in the range of $100 - 300$ MeV in the nuclear interior. This deviation from the G-parity may be caused by many-body effects and by the annihilation of the $\bar{p}$ in the nucleus. Therefore, we use scaled antiproton–meson coupling constants in our calculations

$$g_{\sigma\bar{p}} = \xi\, g_{\sigma N}, \quad g_{\omega\bar{p}} = -\xi\, g_{\omega N}, \quad g_{\rho\bar{p}} = \xi\, g_{\rho N} \ , \tag{2.25}$$

where the parameter ξ is from interval $\langle 0, 1\rangle$ and is considered to have the same value for all fields involved.

The couplings of the vector mesons ω and ρ to hyperons were determined using SU(6) symmetry relations [28, 29, 30]. The values of σ coupling constants were fitted to yield empirical hyperon potentials in the nuclear medium [28, 31, 32, 33]. The coupling constants for the Λ, Σ and Ξ hyperons are as follows:

$$\begin{aligned} g_{\sigma\Lambda} &= 0.621 g_{\sigma N}, \qquad g_{\omega\Lambda} = 2/3 g_{\omega N}, \qquad g_{\rho\Lambda} = 0 \ , \\ g_{\sigma\Sigma} &= 0.5 g_{\sigma N}, \qquad g_{\omega\Sigma} = 2/3 g_{\omega N}, \qquad g_{\rho\Sigma} = 2/3 g_{\rho N} \ , \\ g_{\sigma\Xi} &= 0.299 g_{\sigma N}, \qquad g_{\omega\Xi} = 1/3 g_{\omega N}, \qquad g_{\rho\Xi} = 2/3 g_{\rho N} \ . \end{aligned} \tag{2.26}$$

To obtain the antihyperon–meson couplings we applied again the G-parity transformation to hyperon–meson couplings. The ω meson reverses its sign and becomes attractive. This again indicates that antihyperons would be bound considerably deeper in the nucleus than hyperons. Especially, the Σ hyperon is unbound in the nucleus while the $\bar{\Sigma}$ is bound very strongly in our model (see Fig. 3.15).

2.6 Parametrizations used in the RMF model

The relativistic mean-field model represents an effective theory that contains several parameters which need to be adjusted phenomenologically. These parameter sets, which define the masses of meson fields and meson–nucleon coupling constants, are obtained by fitting nuclear matter and finite nuclei properties (saturation point, binding energies, RMS radii, ...). Basically, there are two groups of parametrizations: linear and nonlinear. The linear models [34] have advantage in their simplicity and numerical stability. They describe reasonably well finite nuclei and nuclear matter saturation properties. However, they yield too large nuclear compressibility ($K \sim 500$ MeV). The nonlinear parametrizations contain extra nonlinear terms for the scalar σ field and vector ω field (and extra parameters g_2, g_3 and d). The nonlinear RMF models give very good description of nuclear matter properties as well as the characteristics of finite nuclei [35, 36]. In our calculations, we employed the nonlinear parameter sets TM1 (for heavier nuclei) and TM2 (for light nuclei) introduced by Sugahara and Toki [37]. For the density dependent model we adopted the TW99 parameter set [38]. It is capable of describing the nuclear properties in similar fashion as the nonlinear parametrizations. The parameter sets TM1, TM2 and TW99 are listed in Table 2.1.

Table 2.1: The parameters of the TM1, TM2 and TW99 models.

	TM1	TM2	TW99		
m_N[MeV]	938	938	939	a_σ	1.365469
m_σ [MeV]	511.198	526.443	550	b_σ	0.226061
m_ω [MeV]	783	783	783	c_σ	0.409704
m_ρ [MeV]	770	770	763	d_σ	0.901995
$g_{\sigma N}$	10.0289	11.4694	10.7285	a_ω	1.402488
$g_{\omega N}$	12.6139	14.6377	13.2902	b_ω	0.172577
$g_{\rho N}$	9.2644	9 .3566	7.3220	c_ω	0.344293
g_2 [fm^{-1}]	-7.2325	-4.4440	0	d_ω	0.983955
g_3	0.6183	4.6076	0	a_ρ	0.515000
d	71.3075	84.5318	0	-	-

Chapter 3

Results

We performed self-consistent RMF calculations of antibaryon–nucleus bound states. We added $\bar{p}$, $\bar{\Lambda}$, $\bar{\Sigma}$, $\bar{\Xi}$ into the $1s_{1/2}$ state of the following nuclei: ^{16}O, ^{40}Ca, ^{90}Zr and ^{208}Pb, and examined the properties of such systems. We calculated nuclear binding energies, nuclear and $\bar{p}$ density distributions, RMS radii and single particle energies. We performed static as well as dynamical calculations. In the static case, the rearrangement of the nucleus due to the presence of the antibaryon was neglected (the source terms for antibaryons were not added into the right hand sides of the Klein–Gordon equations (2.11)). In the dynamical case, the polarization of the nuclear core caused by the antibaryon, as well as the dynamical influence of the nuclear medium on the antibaryon, were considered.

In this work, we will denote $^{A}\mathrm{X}_{\bar{B}}$ the nucleus ^{A}X with one antibaryon $\bar{B}$.

In the first part of this chapter, the results of the calculations of the systems $^{16}\mathrm{O}_{\bar{p}}$, $^{40}\mathrm{Ca}_{\bar{p}}$, $^{90}\mathrm{Zr}_{\bar{p}}$ and $^{208}\mathrm{Pb}_{\bar{p}}$ for scaling factor $\xi = 0.25, 0.5, 0.75, 1$ are discussed. The absorption of the $\bar{p}$ in the nucleus is not considered in this section. The results of calculations with constant nucleon–meson couplings and density–dependent couplings are compared. The annihilation of the $\bar{p}$ in a nucleus is studied in Section 3.2. In the last section of this chapter, the calculations of nuclei with antihyperons $\bar{\Lambda}$, $\bar{\Sigma}$ and $\bar{\Xi}$ are presented.

3.1 Interaction of $\bar{p}$ with nuclei

In this section, we will demonstrate that the antiproton embedded in the nucleus interacts very strongly with the nucleons of the core. The mean fields acting on both the antiproton and nucleons become sizeable, which causes considerable changes in the nuclear structure. In Figure 3.1, the scalar and vector potentials acting

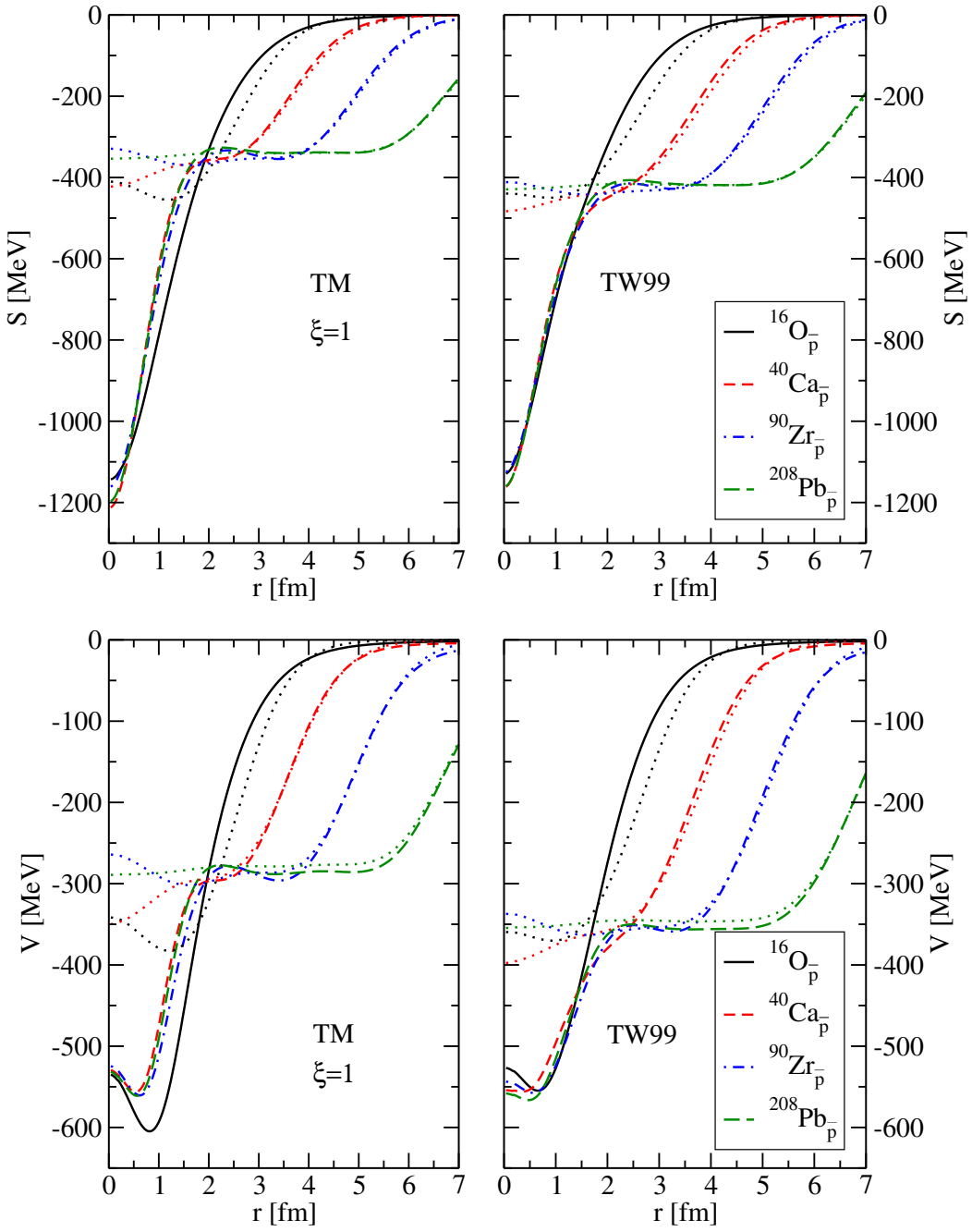

Figure 3.1: The scalar (top) and vector (bottom) potentials felt by the $\bar{p}$ in various nuclei, calculated for $\xi = 1$ in the TM (left) and TW99 (right) model. The dotted lines correspond to the scalar and vector potentials (shown with reversed sign) in ^{16}O, ^{40}Ca, ^{90}Zr and ^{208}Pb.

on $\bar{p}$ in the systems $^{16}O_{\bar{p}}$, $^{40}Ca_{\bar{p}}$, $^{90}Zr_{\bar{p}}$, and $^{208}Pb_{\bar{p}}$ are plotted. The calculations were done for both parametrizations TM and TW99 and for $\xi = 1$. The scalar and vector potentials for $\bar{p}$ are both attractive due to the G-parity transformation. We also present the scalar and vector potentials in ordinary nuclei for comparison

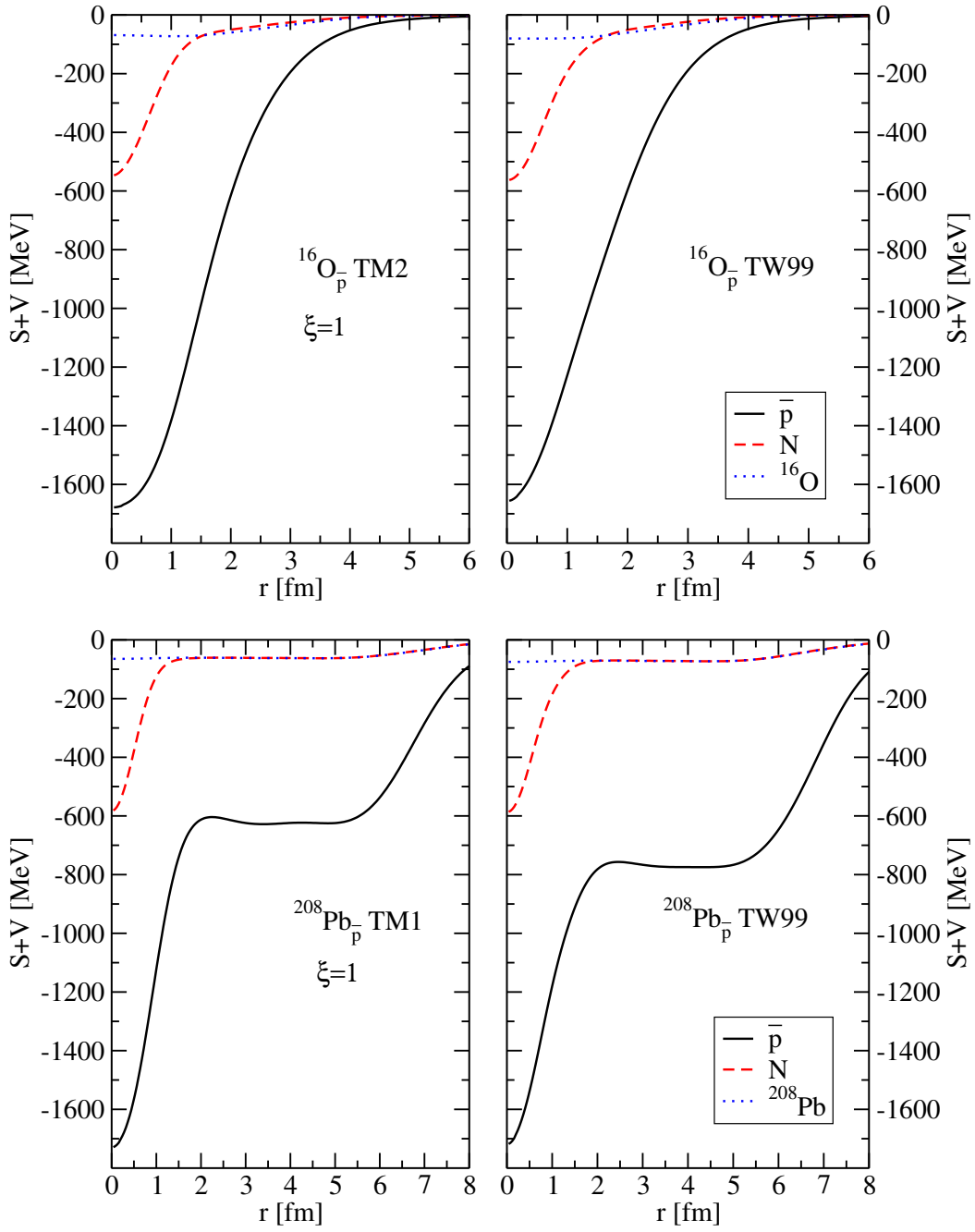

Figure 3.2: The total potential acting on the antiproton ($\bar{p}$) and nucleon (N) in $^{16}O_{\bar{p}}$ (top) and $^{208}Pb_{\bar{p}}$ (bottom), calculated for $\xi = 1$ in the TM (left) and TW99 (right) model. The total potential felt by a nucleon in ^{16}O and ^{208}Pb is plotted for comparison.

(it is to be noted that the vector potential is displayed with reversed sign). We observe extremely deep $\bar{p}$ potentials, particularly in the central region of the nucleus ($r \leq 2$ fm), the depth of the vector potential being about half of the scalar one. This corresponds with the position of the antiproton in a nucleus, which is found to

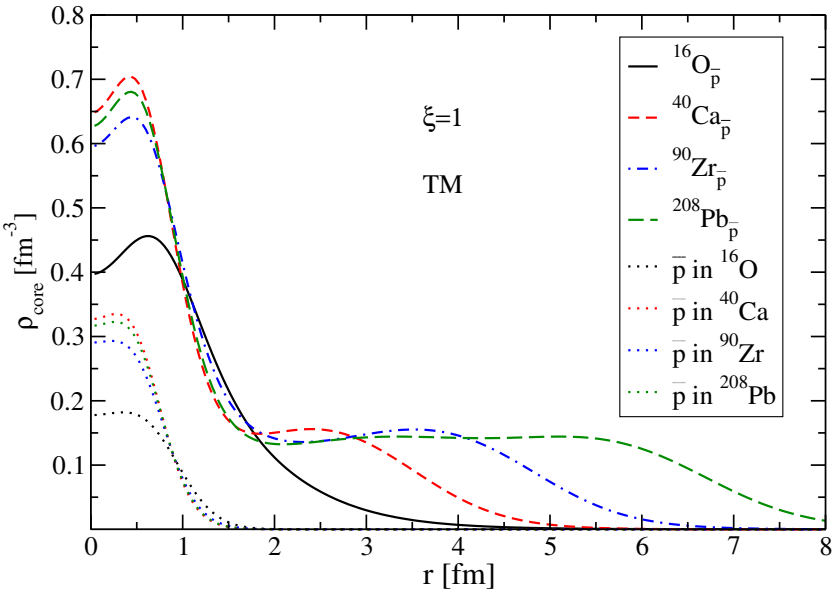

Figure 3.3: The nucleon and antiproton densities in $^{16}O_{\bar{p}}$, $^{40}Ca_{\bar{p}}$, $^{90}Zr_{\bar{p}}$ and $^{208}Pb_{\bar{p}}$, calculated for $\xi = 1$ in the TM model.

be localized in the very center of the core. At larger distances, the scalar and vector potentials are comparable with the corresponding ones in ordinary nuclei, especially in heavier systems like $^{40}Ca_{\bar{p}}$, $^{90}Zr_{\bar{p}}$ and $^{208}Pb_{\bar{p}}$. Both models yield approximately the same depths of the $\bar{p}$ scalar as well as vector potentials. The TW99 model gives slightly shallower potentials; the differences between their depths in the presented nuclei are smaller than in the TM model.

In Fig. 3.2, the total potentials felt by the $\bar{p}$ and nucleons in $^{16}O_{\bar{p}}$ and $^{208}Pb_{\bar{p}}$ are plotted. They were calculated for $\xi = 1$ within the TM and TW99 model. The total potentials acting on nucleons in ordinary nuclei ^{16}O and ^{208}Pb are shown for comparison. The total depth of the $\bar{p}$ potential in both models is tremendous, around 1700 MeV in the central region of both nuclei. This indicates that the $\bar{p}$ feels strong attraction from surrounding nucleons. And on the contrary, the nucleons feel stronger attraction in the presence of the $\bar{p}$ (compare the dashed and dotted line in the figure). A similar situation holds for $^{40}Ca_{\bar{p}}$, $^{90}Zr_{\bar{p}}$ as well. It implies that a nucleus with an antiproton will be deeply bound in the case of the $\bar{p}$ couplings with exact G-parity symmetry.

The nuclear density distribution together with the corresponding $\bar{p}$ density calculated for $\xi = 1$ in the TM model are shown in Fig. 3.3. We can see that the $\bar{p}$ is localized in the center of each nucleus up to ~ 1.5 fm and there is a corresponding increase of the core density distribution in the central region for all nuclei. The nucleons are compressed in the central region since they are strongly attracted by

the antiproton.

In Fig. 3.4, the nuclear density distribution in $^{16}O_{\bar{p}}$ and $^{208}Pb_{\bar{p}}$ is plotted as a function of the scaling parameter ξ for both RMF models. The nuclear density in ^{16}O and ^{208}Pb is shown for comparison. In both $\bar{p}$ nuclei, there is a significant rise in the central nuclear density with increasing parameter ξ. We witness some sort of saturation for $\xi = 0.75$, then the density slightly decreases. The saturation can be explained by the growth of the repulsive force, mediated by the ω field, between nucleons as they get close to each other. This saturation appears in both models. The central density in a nucleus with the antiproton in the $1s_{1/2}$ reaches $3-4$ times the normal nuclear density. An interesting issue is to examine to what extent is the nucleus affected by the antiproton. In the case of light ^{16}O, the presence of the $\bar{p}$ affects the entire nucleus. On the other hand, in ^{208}Pb, the antiproton influences only the central part of the nucleus up to ~ 2 fm. The outer region of the nucleus remains unchanged, the nucleons here are almost unaffected by the presence of the antiproton. It is a consequence of the short range of the $\bar{p}$N interaction. There are apparent differences between the TM and TW99 model. In the TM2 model, the central density in $^{16}O_{\bar{p}}$ is much more lower than in the TW99 model for all ξ since the latter model gives a lower value of nuclear compressibility ($K = 240$ MeV) than the former one ($K = 344$ MeV). Therefore, the nucleons are allowed to get closer to each other and the nuclear density increases more significantly. On the other hand, the nuclear density distribution in the central region of $^{208}Pb_{\bar{p}}$ is similar in both models. The nuclear compressibility of the TM1 model ($K = 281$ MeV) is now closer to the TW99 model. Moreover, the $\bar{p}$ potential in the central region of $^{208}Pb_{\bar{p}}$ is slightly shallower for the TW99 model which affects also the density distributions. This is illustrated in the lower part of Fig. 3.5, where the $\bar{p}$ densities calculated within the TM1 and TW99 models are compared.

In Fig. 3.5, we present the $\bar{p}$ density distribution in $^{16}O_{\bar{p}}$ and $^{208}Pb_{\bar{p}}$ for different values of ξ, calculated in the TM and TW99 model. The $\bar{p}$ density in both nuclei gradually increases with an increasing value of the parameter ξ up to $\xi = 0.5$ when the $\bar{p}$ density reaches its maximum and then starts to decrease until $\xi = 1$. In the RMF model, the nucleon in a nucleus moves in mean-fields created by *ALL* nucleons including itself. It means that the nucleon feels a kind of "attraction" as well as "repulsion" from itself. In an ordinary nucleus, this effect is negligible (and decreases with increasing nucleon number A). However, while the potential acting on a nucleon in an ordinary nucleus is about 50 MeV deep, the scalar and vector potentials acting on the antiproton are both attractive and much deeper, see Fig. 3.1. The effect of the $\bar{p}$ self-interaction then becomes pronounced (note that the $\bar{p}$ vector self-interaction is repulsive). In order to exclude the $\bar{p}$ self-interaction we

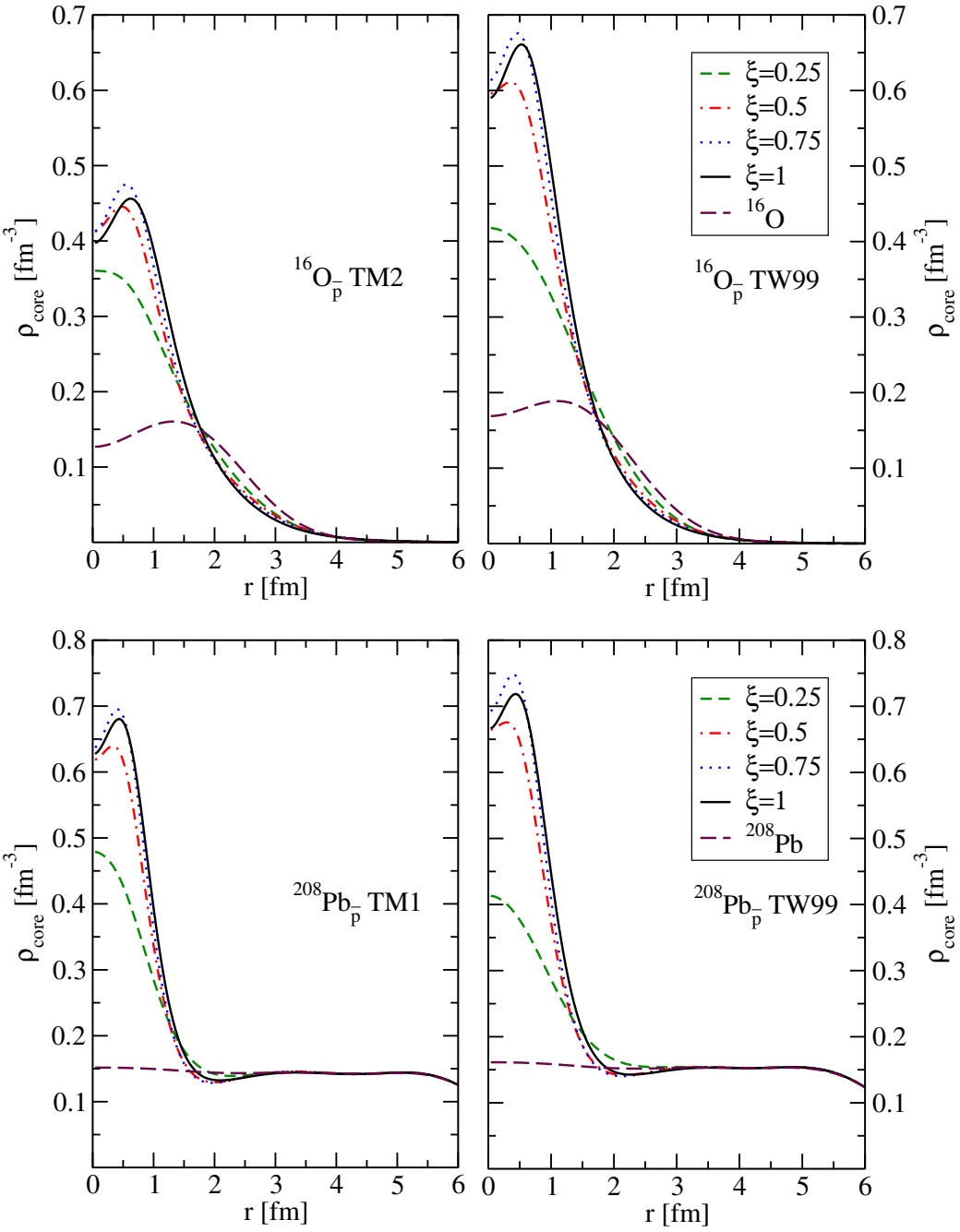

Figure 3.4: The nucleon density distribution in $^{16}O_{\bar{p}}$ (top) and $^{208}Pb_{\bar{p}}$ (bottom), calculated for different values of the parameter ξ in the TM and TW99 model.

modified our computing program correspondingly. In Fig. 3.6, we can see the density distribution of the $\bar{p}$ in $^{16}O_{\bar{p}}$ and $^{208}Pb_{\bar{p}}$ in the TM model compared with density distribution of the $\bar{p}$ in the same nuclei with excluded $\bar{p}$ self-interaction. When the $\bar{p}$ self-interaction is excluded, the $\bar{p}$ density increases with increasing value of the parameter ξ and reaches much higher values. It has to be mentioned that the effect of the $\bar{p}$ self-interaction starts to be dominant for $\xi \sim 0.5$. Therefore, the $\bar{p}$ density

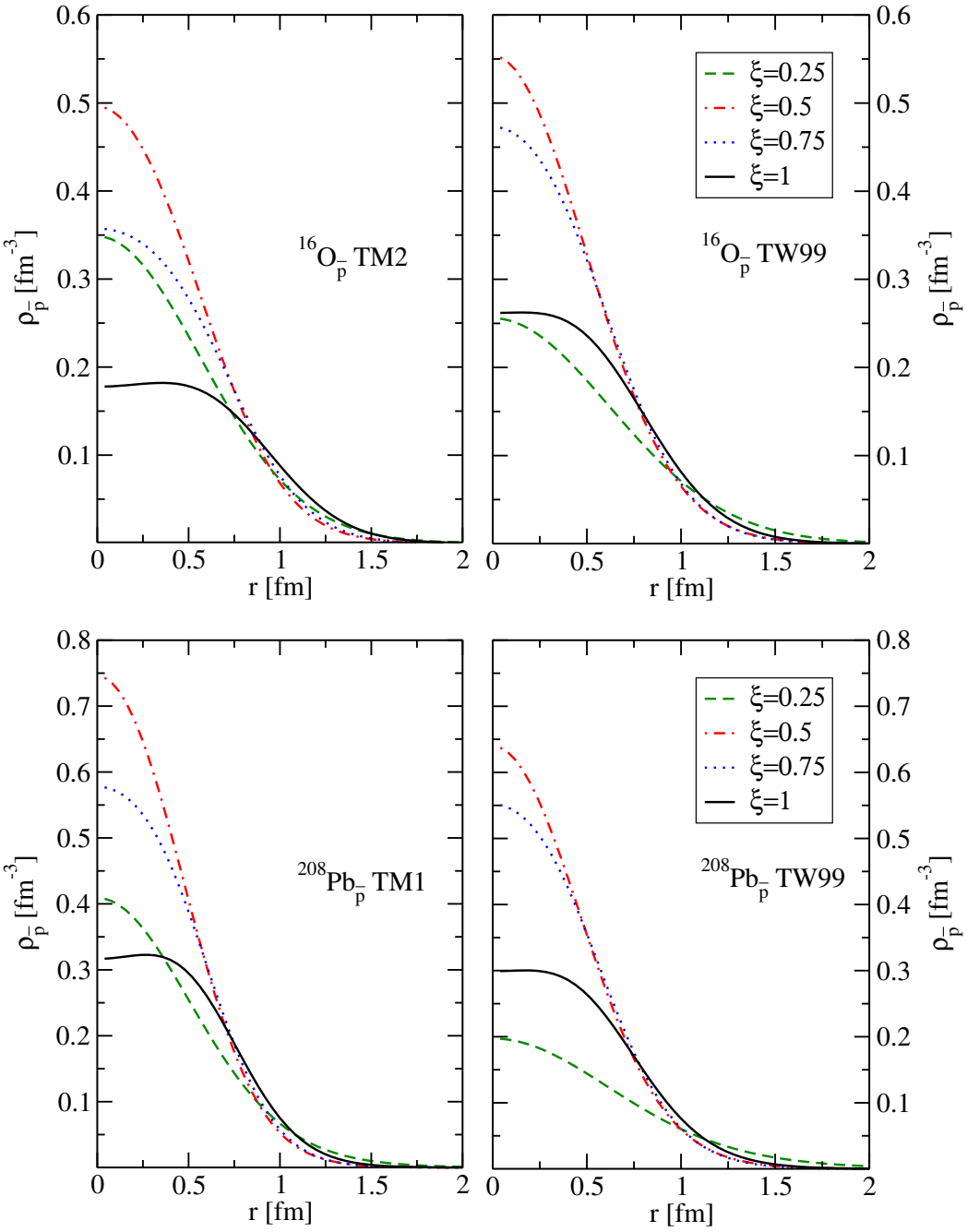

Figure 3.5: The density distribution of the $\bar{p}$ in $^{16}O_{\bar{p}}$ (top) and $^{208}Pb_{\bar{p}}$ (bottom), calculated for different values of the parameter ξ in the TM and TW99 model.

distribution in Fig. 3.5 saturates at this value of ξ. For lower values of the scaling parameter ξ, the effect is less important. The core density in a nucleus where the $\bar{p}$ self-interaction is eliminated reaches higher values, as well, and the whole system is more bound (up to 15%). One should object that all calculation from now on should be performed without the $\bar{p}$ self-interaction. However, as will be shown in the next section, the information from $\bar{p}$ atoms tell us that the strength of the realistic

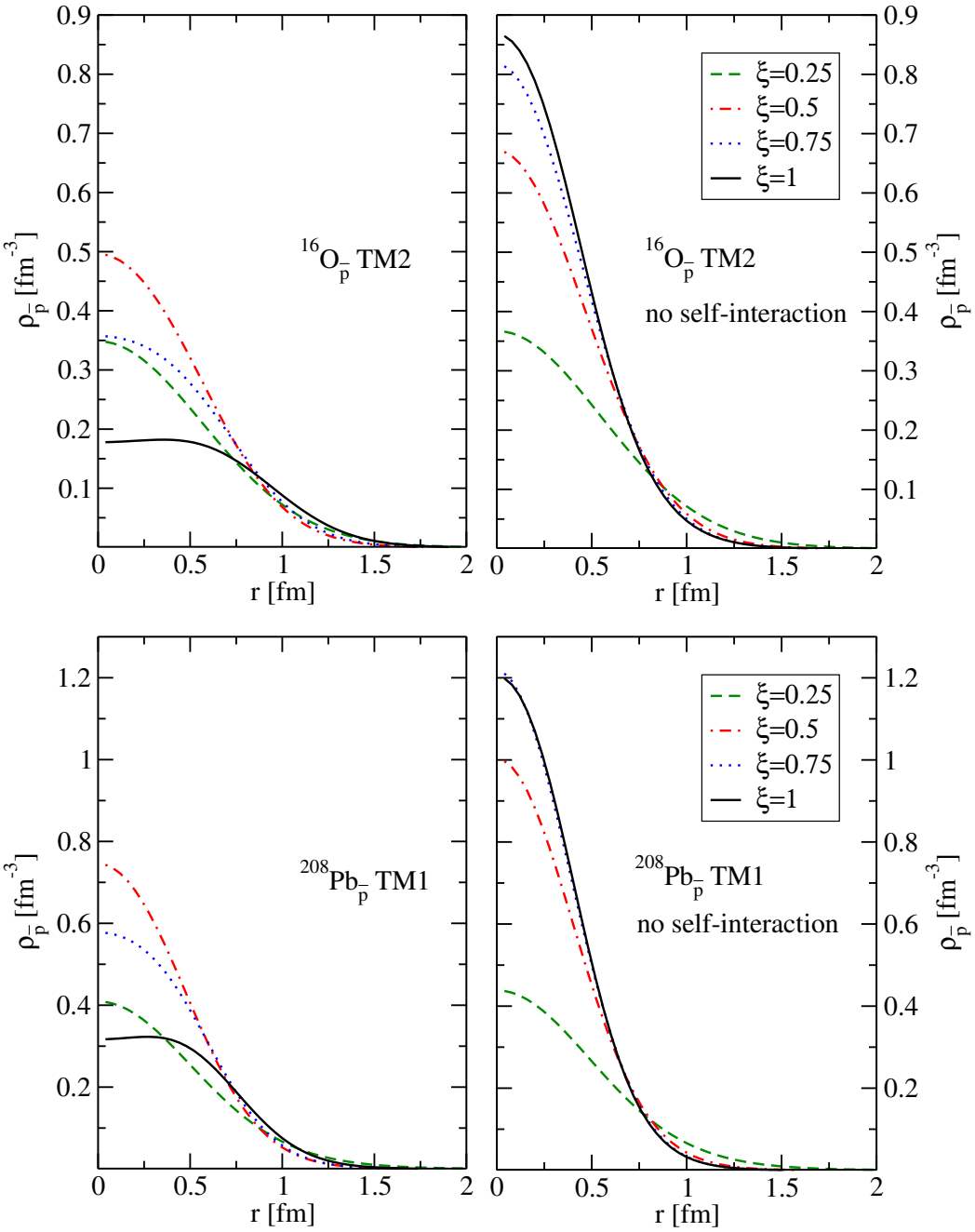

Figure 3.6: The density distribution of the $\bar{p}$ in $^{16}O_{\bar{p}}$ (top) and $^{208}Pb_{\bar{p}}$ (bottom), calculated for different values of the parameter ξ in the TM model with (left) and without (right) the $\bar{p}$ self-interaction.

$\bar{p}$–nucleus interaction corresponds to $\xi \simeq 0.2 - 0.3$. For this scaling, the effect of the $\bar{p}$ self-interaction is negligible.

The difference between the proton and neutron densities (the isovector density $\Delta\rho = \rho_p - \rho_n$) in $^{16}O_{\bar{p}}$ calculated within the TM2 and TW99 model is displayed in Fig. 3.7 for various values of ξ. In the case of the TM2 model, the proton density

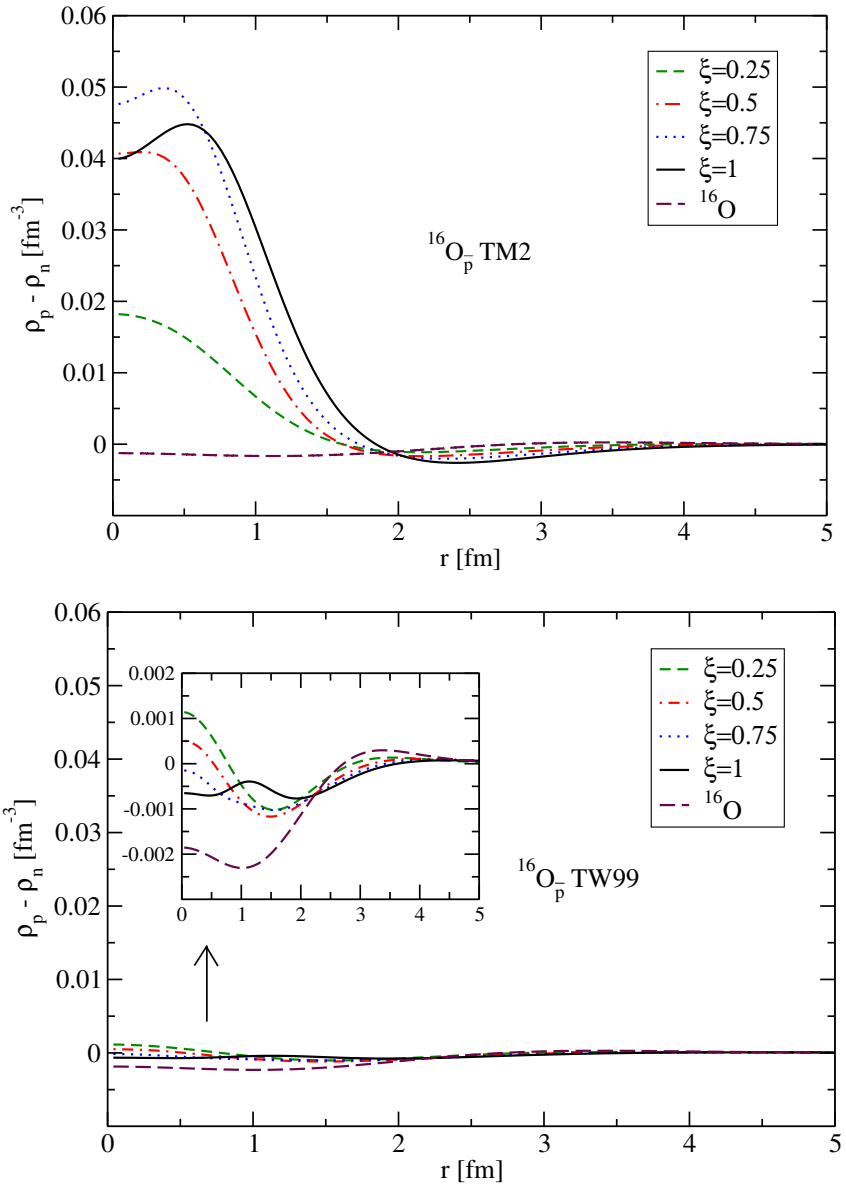

Figure 3.7: The difference between the proton and neutron densities $\Delta\rho = \rho_p - \rho_n$ in $^{16}O_{\bar{p}}$, calculated for different values of the parameter ξ within the TM2 (top) and TW99 (bottom) model. The case of ^{16}O is shown for comparison.

becomes higher than the neutron density in the center of the nucleus. There is an evident massive rearrangement of the nuclear structure due to the presence of the antiproton. Protons are more concentrated around the $\bar{p}$ than neutrons because they feel strong isovector and Coulomb attraction from the antiproton. On the other hand, neutrons feel isovector repulsion due to the same isospin projection as $\bar{p}$. The rearrangement of the nucleus is significant in region up to ~ 2 fm. This corresponds with the antiproton location in the nucleus. In the density–dependent model TW99, we see only a minor effect of the proton and neutron rearrangement

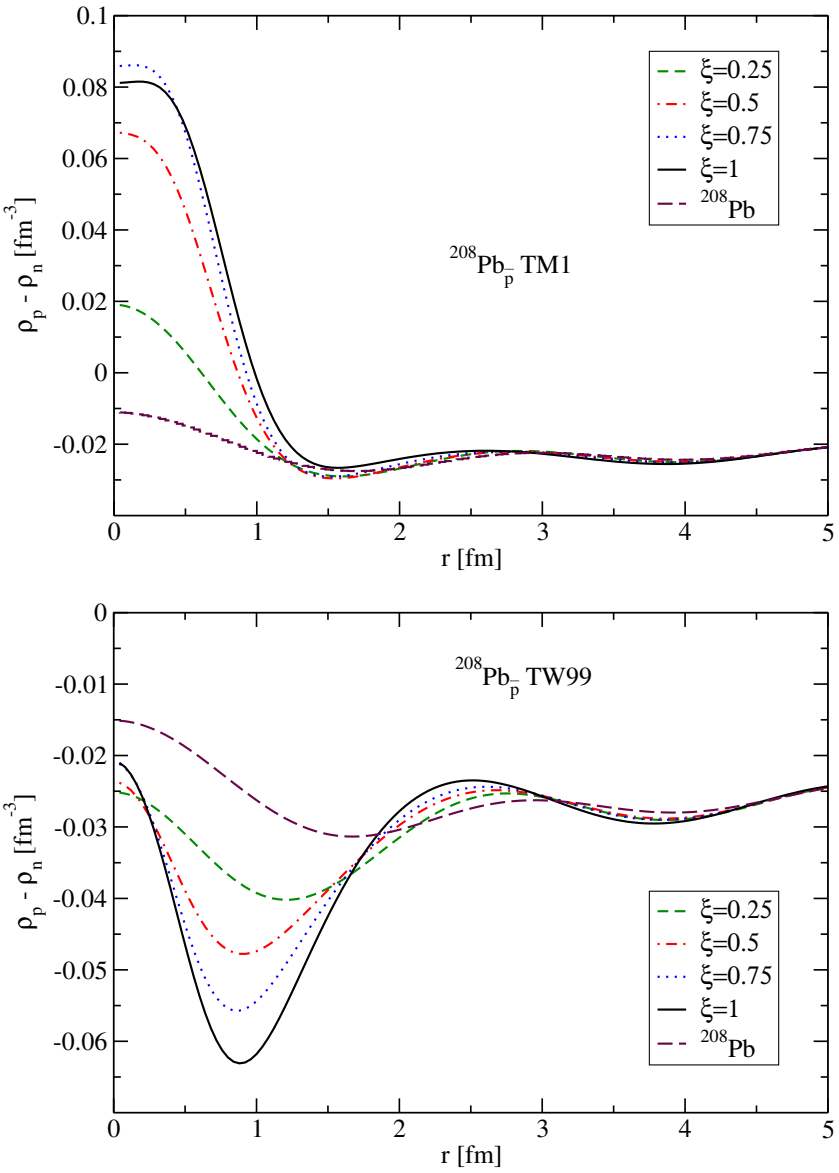

Figure 3.8: The difference between the proton and neutron densities $\Delta\rho = \rho_p - \rho_n$ in $^{208}\mathrm{Pb}_{\bar{p}}$, calculated for different values of the parameter ξ within the TM1 (top) and TW99 (bottom) model. The case of ^{208}Pb is shown for comparison.

in the center of the nucleus $^{16}\mathrm{O}_{\bar{p}}$. However, when we look closer, it is more evident that the proton density is slightly higher than the neutron density in the central region, but this difference decreases with increasing value of ξ. This behavior can be explained by the decreasing strength of the nucleon–ρ meson coupling with the increasing nucleon density. As can be seen in Fig. 3.9, the ρ meson coupling drops substantially in the central region of $^{16}\mathrm{O}_{\bar{p}}$ and consequently the strength of the ρ field is smaller. Therefore, protons do not feel such strong isovector attraction and neutrons do not feel such strong isovector repulsion in the center of the nucleus.

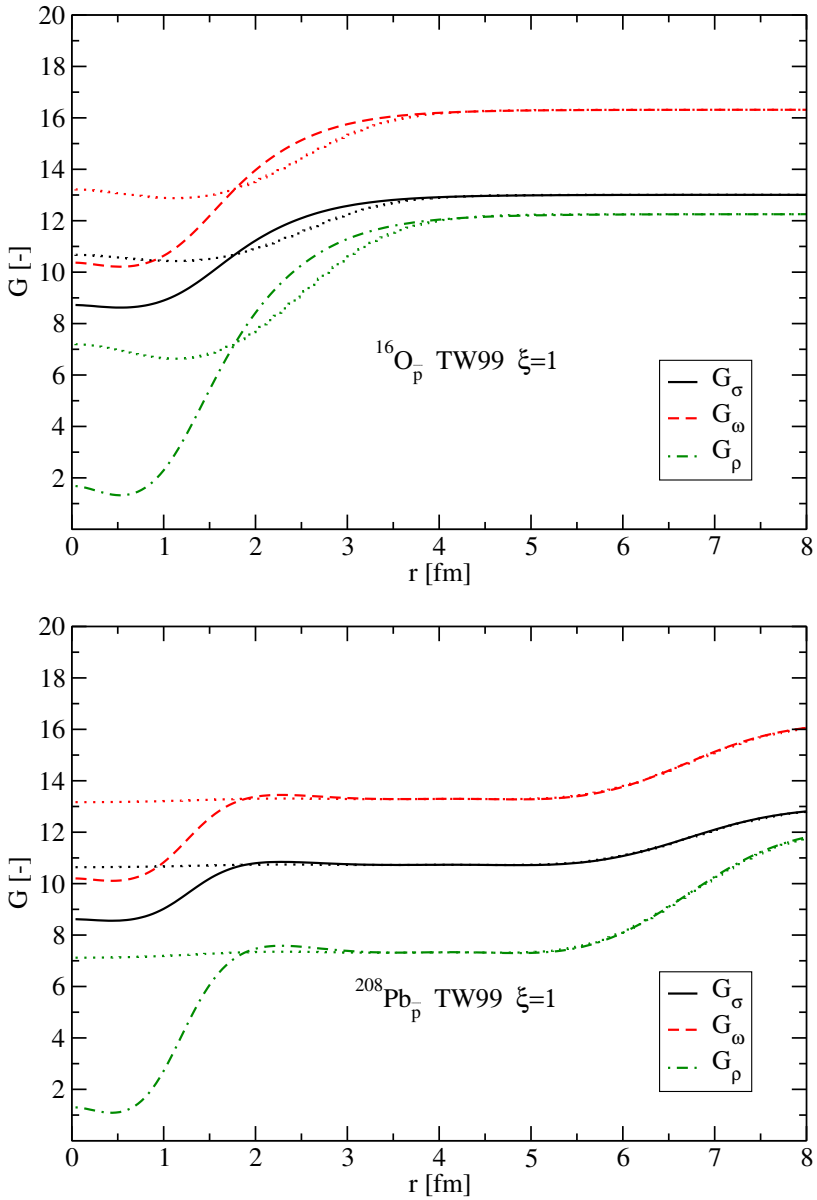

Figure 3.9: The dependence of the density dependent coupling constants on radial coordinate r in $^{16}O_{\bar{p}}$ and $^{208}Pb_{\bar{p}}$ for corresponding meson fields, calculated for $\xi = 1$ in the TW99 model. The radial dependence of the nucleon-meson coupling in normal nuclei (dotted lines) is shown for comparison.

The difference between the proton and neutron densities in $^{208}Pb_{\bar{p}}$ is displayed in Fig. 3.8 for different values of ξ, calculated within the TM1 and TW99 model. There is again a considerable rearrangement of the nuclear structure in the TM1 model. But there is strong polarization of the nucleus for the TW99 model, as well. Since ^{208}Pb contains more neutrons than protons, the effect of the small ρ-meson field in the central region (see Fig. 3.9) causes that neutrons are more concentrated in the center than protons.

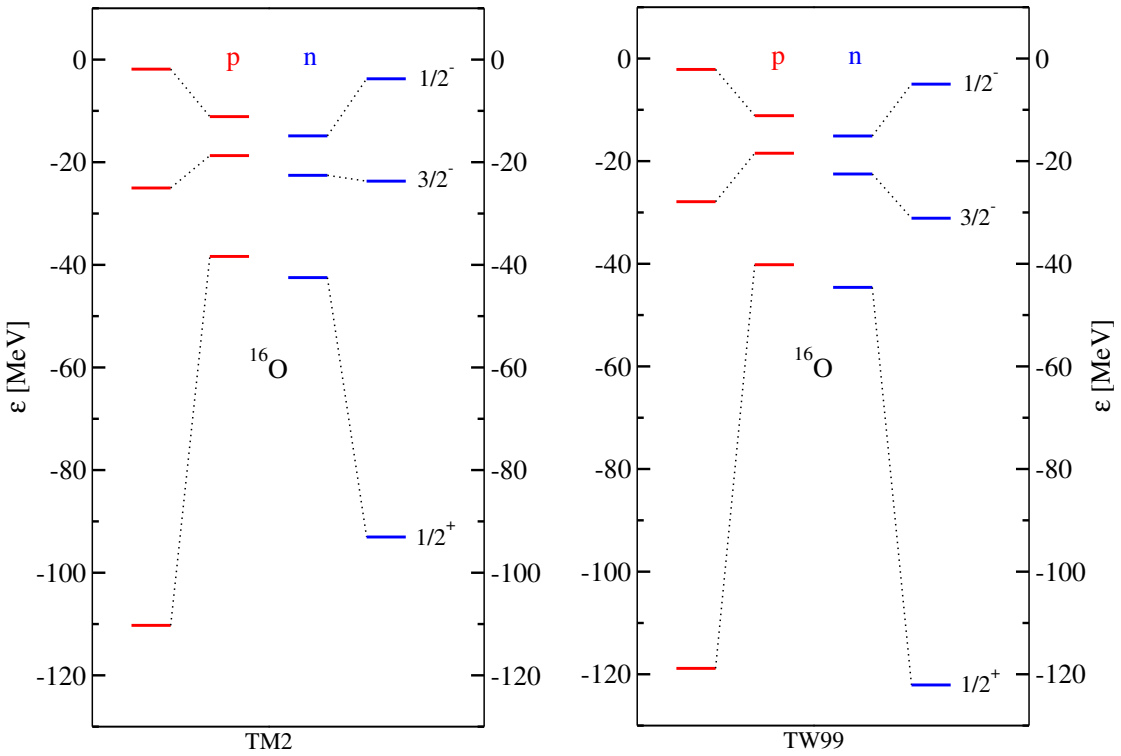

Figure 3.10: The single particle energies of protons (red) and neutron (blue) in $^{16}O_{\bar{p}}$, calculated for $\xi = 1$ in the TM2 (left) and TW99 (right) model. The single particle energies of protons and neutrons in ^{16}O are displayed in the middle of each graph.

The single particle energies of protons and neutrons in $^{16}O_{\bar{p}}$ calculated within the TM2 and TW99 model are displayed in Fig. 3.10 for $\xi = 1$. We can observe that protons and neutrons in the $1s_{1/2}$ state are bound really deeply in the $\bar{p}$ nucleus. There is noticeable influence of the ρ meson. In the TM2 model, protons are more bound than neutrons because of the isovector attraction which is stronger than Coulomb repulsion. On the other hand, protons and neutrons in the density dependent model are bound similarly deep due to the weak ρ-meson field in the central region of the nucleus. The coupling of the repulsive ω field decreases with density faster than the σ coupling (see Fig. 3.9) and this influences the deeper binding of nucleons in the TW99 model. The spin-orbit splitting in the p shell is much larger in $^{16}O_{\bar{p}}$ than in the ordinary nucleus. It is proportional to the sum of the absolute values of the scalar and vector potential (it follows from the nonrelativistic reduction of the Dirac equation) which is considerably larger in the case of $^{16}O_{\bar{p}}$. As a consequence, the nucleons in the $1p_{1/2}$ level in $^{16}O_{\bar{p}}$ are shifted upward and are even less bound than in ^{16}O. The spacing between the $1s$ and $1p$ levels is bigger because of the deeper and narrower potential well in the $\bar{p}$ nucleus.

The single particle energies in $^{90}Zr_{\bar{p}}$ calculated for $\xi = 1$ within the TM1 and TW99 model are shown in Fig. 3.11. The antiproton causes here similar effects as in

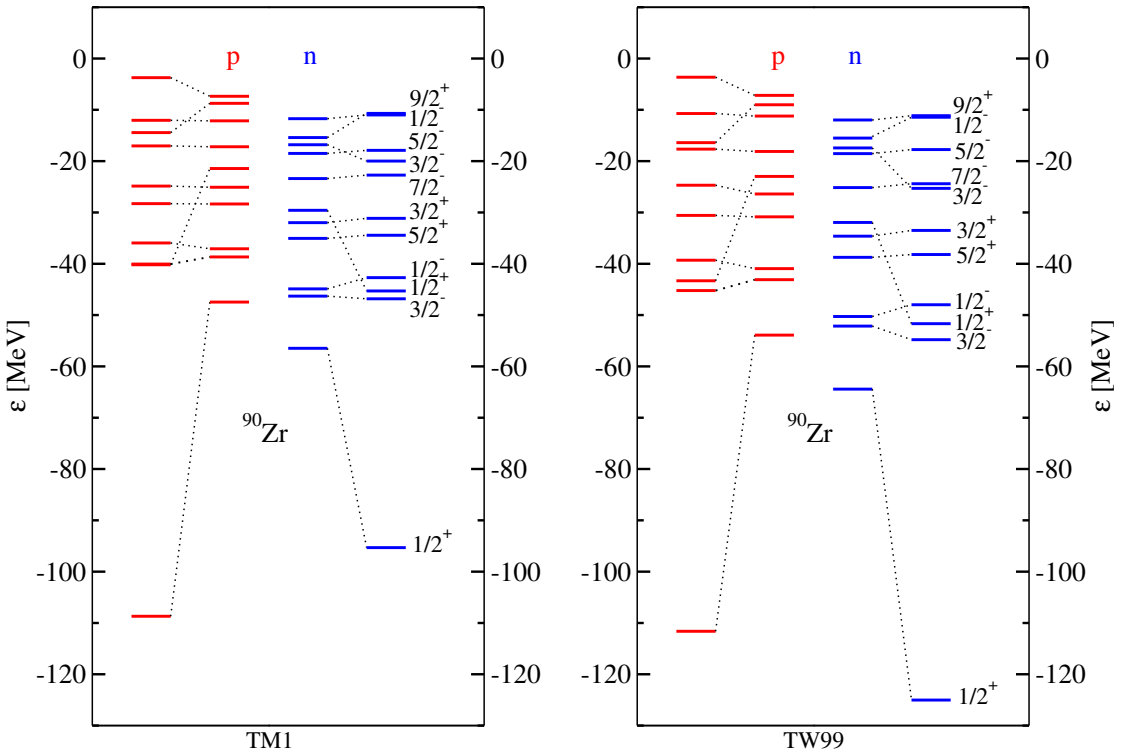

Figure 3.11: The single particle energies of protons (red) and neutron (blue) in $^{90}\mathrm{Zr}_{\bar{p}}$, calculated for $\xi = 1$ in the TM1 (left) and TW99 (right) model. The single particle energies of protons and neutrons in ^{90}Zr are displayed in the middle of each graph.

$^{16}\mathrm{O}_{\bar{p}}$. The large spin-orbit splitting even results in the rearrangement of the p, d and f single particle levels in $^{90}\mathrm{Zr}_{\bar{p}}$. The single particle energies of protons and neutrons in the $1s_{1/2}$ state are again considerable. However, the higher nucleon energy levels are almost unchanged by the presence of the $\bar{p}$. It is due to the short range of the $\bar{p}$N interaction.

Table 3.1: The $\bar{p}$ $1s$ single particle energies $E_{\bar{p}}$, total binding energies B, and binding energies per particle B/A (in MeV) in $\bar{p}$ nuclei, calculated *statically* for $\xi = 1$ within the TM and TW99 model (the binding energies of normal nuclei are shown in parentheses).

		$E_{\bar{p}}$	B	B/A
$^{16}O_{\bar{p}}$	TM2	-755.9	-884.2 (-128.6)	-52.0
	TW99	-740.0	-860.4 (-120.6)	-50.6
$^{40}Ca_{\bar{p}}$	TM1	-658.1	-1002.4 (-344.4)	-24.5
	TW99	-786.0	-1111.6 (-325.7)	-27.1
$^{90}Zr_{\bar{p}}$	TM1	-647.6	-1433.3 (-785.7)	-15.8
	TW99	-784.1	-1528.7 (-744.6)	-16.8
$^{208}Pb_{\bar{p}}$	TM1	-623.0	-2257.7 (-1634.8)	-10.8
	TW99	-766.2	-2271.7 (-1505.4)	-10.9

The $\bar{p}$ single particle energies, the total binding energies, and binding energies per particle in selected nuclei, calculated statically with $\xi = 1$ within the TM and TW99 model, are shown in Table 3.1. The $\bar{p}$ single particle energies represent the solution of the corresponding Dirac equation. In the static calculations, the single particle energies are identical with the $\bar{p}$ binding energies and their absolute values decrease with increasing A in the TM model. In the TW99 model, $^{16}O_{\bar{p}}$ violates this sequence. The binding energies of the $\bar{p}$ nuclei are substantially larger than the binding energies of the corresponding normal nuclei. The considerable compression of a nucleus caused by the $\bar{p}$ manifests itself by the binding energies per particle B/A which are extremely large particularly in lighter nuclei (and decrease with A).

In Table 3.2, we present the $\bar{p}$ $1s$ single particle energies, $\bar{p}$ binding energies, total binding energies, and binding energies per particle in $^{16}O_{\bar{p}}$, $^{40}Ca_{\bar{p}}$, $^{90}Zr_{\bar{p}}$ and $^{208}Pb_{\bar{p}}$. The presented quantities are results of the dynamical calculations with $\xi = 1$ within the TM and TW99 model. The binding energy of a $\bar{p}$ nucleus considerably increases in both models. The TM model gives similar $\bar{p}$ single particle energies as the TW99 model (except $^{16}O_{\bar{p}}$). On the other hand, the $\bar{p}$ binding energies in the TM model are somewhat higher. Both models predict quite similar values of the energies $E_{\bar{p}}$, as well as $B_{\bar{p}}$ in all nuclei under consideration (except the TM2 model in the case of $^{16}O_{\bar{p}}$). When we compare the results of the static and dynamical calculations in Tables 3.1 and 3.2, we see that the $\bar{p}$ single particle energies calculated dynamically are approximately twice as high as those calculated statically. The total binding energies in dynamical calculations are considerably higher, as well. Further, there is a significant difference between the $\bar{p}$ single particle energies and the $\bar{p}$ binding

Table 3.2: The $\bar{p}$ $1s$ single particle energies $E_{\bar{p}}$, total binding energies B, antiproton binding energies $B_{\bar{p}}$, and binding energies per particle B/A (in MeV) in $\bar{p}$ nuclei, calculated *dynamically* for $\xi = 1$ within the TM and TW99 model.

		$E_{\bar{p}}$	$B_{\bar{p}}$	B	B/A
$^{16}O_{\bar{p}}$	TM2	-1212.4	-1131.3	-1259.9	-74.1
	TW99	-1130.9	-993.5	-1114.1	-65.5
$^{40}Ca_{\bar{p}}$	TM1	-1097.2	-1019.9	-1364.3	-33.3
	TW99	-1107.5	-989.2	-1314.9	-32.1
$^{90}Zr_{\bar{p}}$	TM1	-1119.6	-1012.9	-1798.6	-19.8
	TW99	-1130.0	-987.6	-1732.2	-19.4
$^{208}Pb_{\bar{p}}$	TM1	-1107.5	-1016.4	-2651.2	-12.7
	TW99	-1124.9	-990.3	-2495.7	-11.9

energies in the dynamical calculations. This is due to the polarization effects in nuclei caused by the antiproton. The binding energies per particle reach tremendous values. We can see that the highest energy per particle is in $^{16}O_{\bar{p}}$, with $B/A = 74$ and 65 MeV for the TM2 and TW99 model, respectively. The binding energy per particle decreases with increasing nucleon number A.

Table 3.3 shows the total binding energies, $\bar{p}$ $1s$ single particle and binding energies together with the difference between the $\bar{p}$ single particle and binding energies, calculated for different values of the scaling parameter ξ in $^{16}O_{\bar{p}}$ within the TM2 model. We can observe how the binding energy of the nucleus, and the $\bar{p}$ single particle and binding energy increase with increasing value of the parameter ξ. Moreover, the difference between the $\bar{p}$ single particle energy and the $\bar{p}$ binding energy is getting larger with ξ. It shows how big are the polarization effects in the nucleus.

Table 3.3: The total binding energies B, $\bar{p}$ $1s$ single particle energies $E_{\bar{p}}$, antiproton binding energies $B_{\bar{p}}$ and the difference between the single particle energies and binding energies $E_{\bar{p}} - B_{\bar{p}}$ of the $\bar{p}$ (in MeV) in $^{16}O_{\bar{p}}$, calculated dynamically for given values of ξ within the TM2 model.

$^{16}O_{\bar{p}}$ TM2	$\xi = 0.25$	$\xi = 0.5$	$\xi = 0.75$	$\xi = 1$
B	-353.6	-678.5	-994.1	-1259.9
$E_{\bar{p}}$	-265.2	-623.4	-948.6	-1212.4
$B_{\bar{p}}$	-225.0	-549.9	-865.5	-1131.3
$E_{\bar{p}} - B_{\bar{p}}$	-40.3	-73.5	-83.1	-81.1

3.2 $\bar{p}$ annihilation in a nucleus

An inseparable part of the $\bar{p}$–nucleus interaction is the annihilation of the $\bar{p}$ in the nuclear medium. Since the RMF model does not address the absorption of the $\bar{p}$ in the nucleus we adopted the imaginary part of the optical potential in a '$t\rho$' form from the optical model phenomenology:

$$2\mu V_{\rm opt}(r) = -4\pi \left(1 + \frac{\mu}{m_N}\frac{A-1}{A}\right) b_0 \rho(r) \ , \tag{3.1}$$

where μ is the $\bar{p}$–nucleus reduced mass. While the density ρ was treated as a dynamical quantity determined within the RMF model, the parameter b_0 was constrained by fits to $\bar{p}$-atomic data [15].

The global fits to the $\bar{p}$-atomic data give a single value for the imaginary part of b_0, Imb_0 = 1.9 fm for all nuclei considered. Together with the parameter Imb_0 from global fits we adopted a single scaling factor $\xi = 0.2$ for the real part of the $\bar{p}$ potential. However, the fits to the data for particular nuclei give somewhat different parameters: Imb_0 = 0.35 fm for ^{16}O, Imb_0 = 2.0 fm for ^{40}Ca and Imb_0 = 2.5 fm for ^{208}Pb. The corresponding values of the scaling parameter ξ needed to fit the data were $\xi = 0.35, 0.15$ and 0.25 for ^{16}O, ^{40}Ca and ^{208}Pb, respectively.

In our calculations, we added the imaginary part of the optical potential $V_{\rm opt}$ to the real RMF $\bar{p}$ potential and defined the width of the $\bar{p}$ state $\Gamma_{\bar{p}} = 2{\rm Im}E_{\bar{p}}$. We performed calculations for the above sets of parameters Imb_0 and ξ, determined by the fits to $\bar{p}$-atomic data.

The strongly interacting antiproton embedded in the nucleus causes a considerable rise of the nuclear density, which leads to an increased $\bar{p}$ decay width. On the other hand, the antiproton in the nucleus is deeply bound even for $\xi \simeq\ 0.2 - 0.3$. Since the energy available for the annihilation in the nuclear medium is $\sqrt{s} = m_{\bar{p}} + m_N - E_{\bar{p}} - E_N$, the phase space available for the annihilation products is considerably suppressed for the deeply bound $\bar{p}$. Therefore, the width $\Gamma_{\bar{p}}$ is a result of the above two competing effects. In order to incorporate the phase space reduction, we introduced suppression factors. We considered various vacuum $\bar{N}N$ annihilation channels listed together with corresponding thresholds and branching rations B_c in Table 3.4. We used the phase space suppression factors for the vacuum two-body annihilation channels in the form

$$f_{\rm s} = \frac{M_{01}^2}{s}\sqrt{\frac{[s-(m_1+m_2)^2][s-(m_1-m_2)^2]}{[M_{01}^2-(m_1+m_2)][M_{01}^2-(m_1-m_2)^2]}}\Theta(\sqrt{s}-m_1-m_2) \ , \tag{3.2}$$

where m_1, m_2 are the masses of the annihilation products and $M_{01} = m_{\bar{p}} + m_N$.

Table 3.4: The annihilation channels for $\bar{N}N$ at rest in vacuum.

channel	$\sqrt{s}$ [GeV]	B_c [%]
2π	0.27	0.38
3π	0.41	2.5
$\pi\rho$	0.91	5.1
4π	0.54	12.5
$\pi\omega$	0.92	0.6
2ρ	1.54	0.9
5π	0.68	31.0
$\rho\omega$	1.55	2.3
6π	0.82	17.2
$\omega\eta$	1.32	1.5
2ω	1.54	3.0
7π	0.97	5.9

The values of the suppression factors for the annihilation into 3 and more pions were adopted from Ref. [1]. In Fig. 3.12, we can see the phase space suppression factors f_s as a function of the center-of-mass energy $\sqrt{s}$. The imaginary part $\mathrm{Im}V_{\mathrm{opt}}$ was then multiplied by a corresponding suppression factor and branching ratio for each vacuum annihilation channel from Table 3.4.

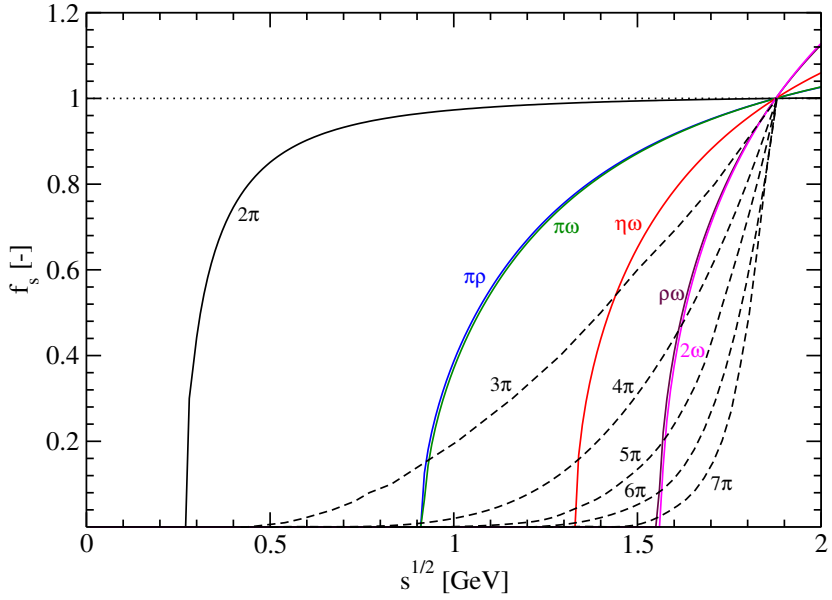

Figure 3.12: The phase space suppression factor f_s for various annihilation channels as a function of the center-of-mass energy $\sqrt{s}$.

Table 3.5: The total binding energies B, $\bar{p}$ $1s$ single particle energies and $\bar{p}$ widths $\Gamma_{\bar{p}}$ (in MeV) in $^{16}O_{\bar{p}}$, calculated for different ξ and Imb_0=1.9 fm within the TM2 model.

SF			
$^{16}O_{\bar{p}}$ TM2	$\xi = 0.2$	$\xi = 0.5$	$\xi = 1$
B	-292.6	-678.5	-1259.9
$E_{\bar{p}}$	-192.3	-623.3	-1212.4
$\Gamma_{\bar{p}}$	145.4	43.1	2.8
no SF			
B	-272.4	-661.8	-1251.9
$E_{\bar{p}}$	-175.6	-605.2	-1202.6
$\Gamma_{\bar{p}}$	552.3	780.0	752.2

In Table 3.5, we present the total binding energies, $\bar{p}$ single particle energies and widths in $^{16}O_{\bar{p}}$, calculated for different values of ξ and Imb_0 = 1.9 fm within the TM2 model. To demonstrate the crucial role of the phase considerations, we show the results of the calculations with (SF) and without (no SF) suppression factors for comparison. The energy of the $\bar{p}$ and the total binding energy increase with the increasing value of the parameter ξ in both cases. The larger is the energy of the $\bar{p}$ in the nucleus the lower is the energy available for annihilation. Consequently, the phase space for annihilation products is significantly reduced which results in a considerably smaller $\bar{p}$ absorption width, which for $\xi = 1$ is only 2.8 MeV. In the case without suppression factors, the $\bar{p}$ widths are really huge, compare $\Gamma_{\bar{p}} = 752$ MeV (no SF) with $\Gamma_{\bar{p}} = 2.8$ MeV (SF). Such a strong $\bar{p}$ absorption contributes to repulsion in the real part of the optical potential and, as a result, the antiproton is less bound than in the case with SF.

The real and imaginary part of the $\bar{p}$ potential calculated for $\xi = 0.35, 0.15, 0.25$ and Imb_0 = 3.5, 2.0, 2.5 fm in $^{16}O_{\bar{p}}$, $^{40}Ca_{\bar{p}}$ and $^{208}Pb_{\bar{p}}$, respectively, are displayed in Fig. 3.13. The quite different scaling factors ξ in the studied nuclei result in considerably different depths of Re$V_{\rm opt}$. In particular, the $\bar{p}$ potential in $^{16}O_{\bar{p}}$ is about 3 times deeper than the $\bar{p}$ potential in $^{40}Ca_{\bar{p}}$. Such a huge difference between the $\bar{p}$ potentials is hard to be explained by a theoretical model and thus seems unrealistic. The differences between the imaginary $\bar{p}$ potential are less pronounced due to the effect of the suppression factors.

In Table 3.6, we present the total binding energies, $\bar{p}$ single particle energies and widths in selected nuclei, corresponding to the $\bar{p}$ potentials shown in Fig. 3.13. The differences between the depths of the potential in Fig. 3.13 result in a sizable

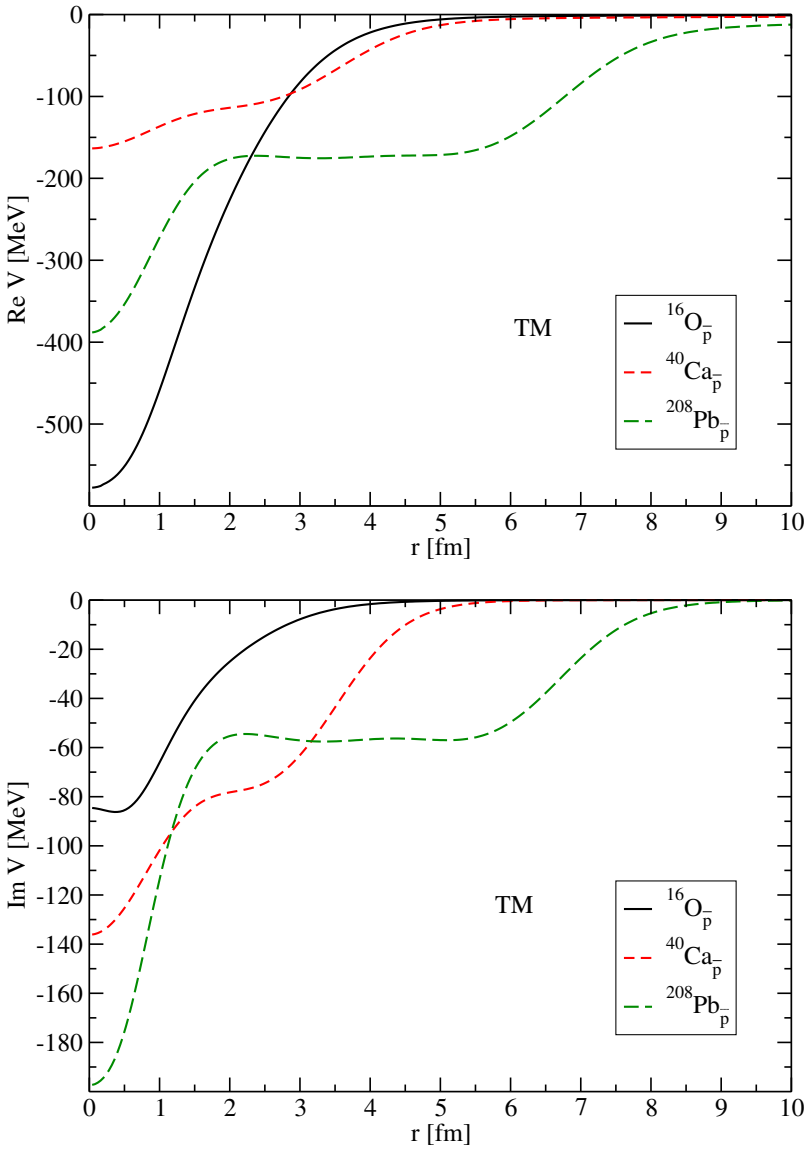

Figure 3.13: The real (top) and imaginary (bottom) part of the $\bar{p}$ potential in $^{16}O_{\bar{p}}$, $^{40}Ca_{\bar{p}}$ and $^{208}Pb_{\bar{p}}$ for $\xi = 0.35, 0.15, 0.25$ and $\mathrm{Im}b_0 = 3.5, 2.0, 2.5$ fm, respectively, calculated dynamically within the TM model.

Table 3.6: The total binding energies B, $\bar{p}$ $1s$ single particle energies $E_{\bar{p}}$ and widths $\Gamma_{\bar{p}}$ (in MeV), calculated self-consistently within the TM model for $\xi = 0.35, 0.15, 0.25$ and $\mathrm{Im}b_0 = 3.5, 2.0, 2.5$ fm.

	$^{16}O_{\bar{p}}$ TM2	$^{40}Ca_{\bar{p}}$ TM1	$^{208}Pb_{\bar{p}}$ TM1
B	-479.8	-438.8	-1817.5
$E_{\bar{p}}$	-409.2	-101.0	-225.5
$\Gamma_{\bar{p}}$	144.8	182.0	269.7

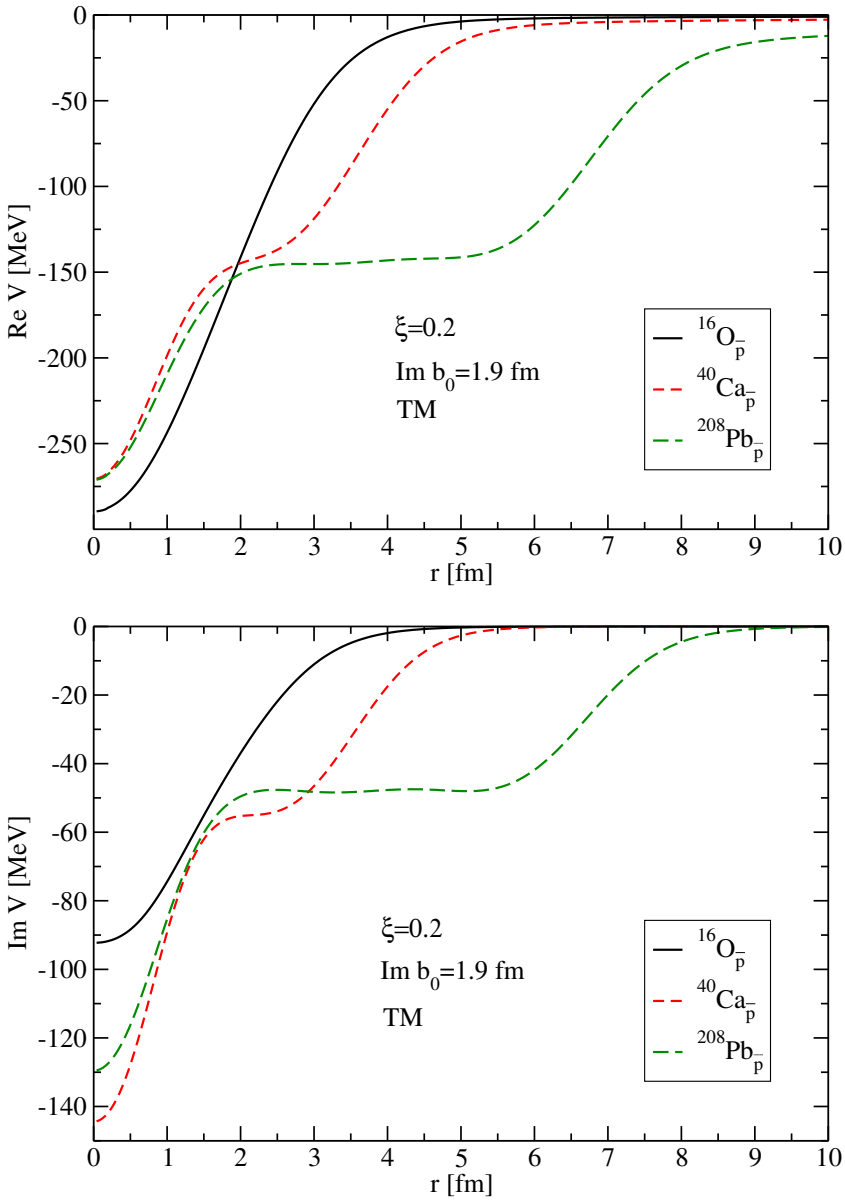

Figure 3.14: The real (top) and imaginary (bottom) part of the $\bar{p}$ potential in $^{16}O_{\bar{p}}$, $^{40}Ca_{\bar{p}}$ and $^{208}Pb_{\bar{p}}$ for $\xi = 0.2$ and $\mathrm{Im}b_0 = 1.9$ fm, calculated dynamically within the TM model.

differences between the $\bar{p}$ single particle energies; $E_{\bar{p}}$ in $^{16}O_{\bar{p}}$ is 4 times larger than the one in $^{40}Ca_{\bar{p}}$ and about twice as large as $E_{\bar{p}}$ in $^{208}Pb_{\bar{p}}$. Moreover, the total binding energy in $^{16}O_{\bar{p}}$ is surprisingly larger than the one in $^{40}Ca_{\bar{p}}$. On the other hand, the widths $\Gamma_{\bar{p}}$, which are controlled by the suppression factors, differ noticeably less from each other, as shown in the last row of the Table 3.6.

Fig. 3.13 and Table 3.6 clearly indicate the insufficiency of the $\bar{p}$-atomic fits to determine the central depth of the $\bar{p}$ potential. Namely the atomic data probe the $\bar{p}$ potential at the nuclear surface and its shape in the interior is a result of extrapola-

Table 3.7: The total binding energies B, $\bar{p}$ $1s$ single particle energies $E_{\bar{p}}$ and widths $\Gamma_{\bar{p}}$ (in MeV), calculated self-consistently within the TM model for $\xi = 0.2$ and Imb_0=1.9 fm.

	$^{16}O_{\bar{p}}$ TM2	$^{40}Ca_{\bar{p}}$ TM1	$^{208}Pb_{\bar{p}}$ TM1
B	-292.6	-477.1	-1774.4
$E_{\bar{p}}$	-192.3	-152.9	-163.1
$\Gamma_{\bar{p}}$	145.4	182.6	169.3

tion within the applied model. From the above reasons we prefer a parametrization determined from the global fits of the $\bar{p}$-atomic data, which yields unified (and reasonable) description of the $\bar{p}$ interaction with nuclei in a large mass range.

In Fig. 3.14, the real and imaginary part of the $\bar{p}$ potential for $^{16}O_{\bar{p}}$, $^{40}Ca_{\bar{p}}$ and $^{208}Pb_{\bar{p}}$ are plotted, calculated dynamically within the TM model for the global parameters $\xi = 0.2$ and Im$b_0 = 1.9$ fm. The depths of the real part of the $\bar{p}$ potential are approximately the same for all considered nuclei and reach nearly 300 MeV. The depths of Im$V_{\rm opt}$ reflect the differences between the densities in the studied nuclei. The absorption potential is the shallowest in $^{16}O_{\bar{p}}$ and the deepest in the $^{40}Ca_{\bar{p}}$. Even if we consider the suppression of the phase space for the annihilation products, the absorptive $\bar{p}$ potential is still fairly strong in the center of a nucleus where the antiproton is localized.

In Table 3.7, we present the total binding energies, $\bar{p}$ single particle energies and widths in selected nuclei, corresponding to the $\bar{p}$ potentials shown in Fig. 3.14. The suppression of the phase space is again taken into account. The $\bar{p}$ single particle energies are close to each other in all nuclei due to the similar depths of Re$V_{\rm opt}$. The $\bar{p}$ widths still remain large despite the considered suppression of the phase space.

In Table 3.8, we compare static and dynamical calculations with real, complex and complex with SF potentials in $^{16}O_{\bar{p}}$ for $\xi = 0.2$ and Im$b_0 = 1.9$ fm within the TM2 model. While the static calculations give about the same values of $E_{\bar{p}}$ and the total binding energy in all three cases, the results of dynamical calculations differ considerably. The polarization of the nucleus is significant even if the absorption of the $\bar{p}$ is involved—the difference between the $\bar{p}$ single particle energies calculated statically and dynamically is up to 55 MeV. In dynamical calculations, the real $\bar{p}$ potential gives the largest $\bar{p}$ energy $E_{\bar{p}}$, while the complex potential without SF yields $E_{\bar{p}}$ about 20 MeV lower due to the "repulsive" effect of the strong absorptive part in $V_{\rm opt}$. The suppression of the phase space for annihilation products reduces significantly the $\bar{p}$ widths (more than 3 times in the case of dynamical calculations) and leads to larger $\bar{p}$ energy $E_{\bar{p}}$, which is comparable with the real case.

Table 3.8: The total binding energies B, $\bar{p}$ $1s$ single particle energies $E_{\bar{p}}$ and widths $\Gamma_{\bar{p}}$ (in MeV) in $^{16}O_{\bar{p}}$, calculated for $\xi = 0.2$ and Imb_0=1.9 fm dynamically (Dyn) and statically (Stat) with the real, complex and complex with SF potentials.

	Real		Complex		Complex SF	
	Dyn	Stat	Dyn	Stat	Dyn	Stat
B	-294.5	-265.5	-272.4	-263.0	-292.6	-264.9
$E_{\bar{p}}$	-193.7	-137.1	-175.6	-134.6	-192.3	-136.6
$\Gamma_{\bar{p}}$	-	-	552.3	293.3	145.4	116.8

It is to be noted that the fully self-consistent calculations of $\bar{p}$ nuclei with a complex potential including suppression factors were performed in this work for the first time ever.

3.3 Interaction of antihyperons with nuclei

We studied the interaction of the $\bar{\Lambda}, \bar{\Sigma}$ and $\bar{\Xi}$ antihyperons with ^{16}O, ^{40}Ca, ^{90}Zr and ^{208}Pb. We added the antihyperon into the $1s_{1/2}$ state and performed self-consistent dynamical calculations within the TM and TW99 models. In these first calculations, we did not consider the absorption of the antihyperon in the nucleus. We rather focused on the polarization effects in the nuclear core caused by the antihyperon.

In this section, we will use the following notation: we will denote the antiparticle to Σ^+ as $\bar{\Sigma}^+$ and the antiparticle to Σ^- as $\bar{\Sigma}^-$. The same convention is used for $\bar{\Xi}$.

In Fig. 3.15, we present the potentials acting on the Λ, Σ^0 and Ξ^0 hyperons in ^{208}Pb, calculated within the TM1 model. The Λ potential is about 30 MeV deep [24], the Ξ^0 potential is even shallower ($\sim$ 15 MeV) [32] and the Σ^0 potential is repulsive in the nuclear interior with a shallow attractive pocket near the nuclear surface [31]. On the other hand, the antihyperon potentials are quite deep due to the G-parity transformation of the ω field which becomes attractive. There is significant increase of the antihyperon potential in the central region of the nucleus (the similar trend was observed in $\bar{p}$ nuclei, see Fig. 3.2). The depth of the potentials indicates that the antihyperons will be bound more deeply in the nucleus than hyperons. The $\bar{\Lambda}$ potential is the deepest due to the strongest coupling to the σ meson field, then follows the $\bar{\Sigma}^0$ with the same coupling to the ω field but much weaker coupling to the σ field. The depth of the $\bar{\Xi}^0$ potential is less than half of the above two potentials since for the Ξ^0 it holds $g_{i\Xi} \approx \frac{g_{i\Lambda}}{2}$, where $i = \sigma, \omega$ (see equation (2.26)).

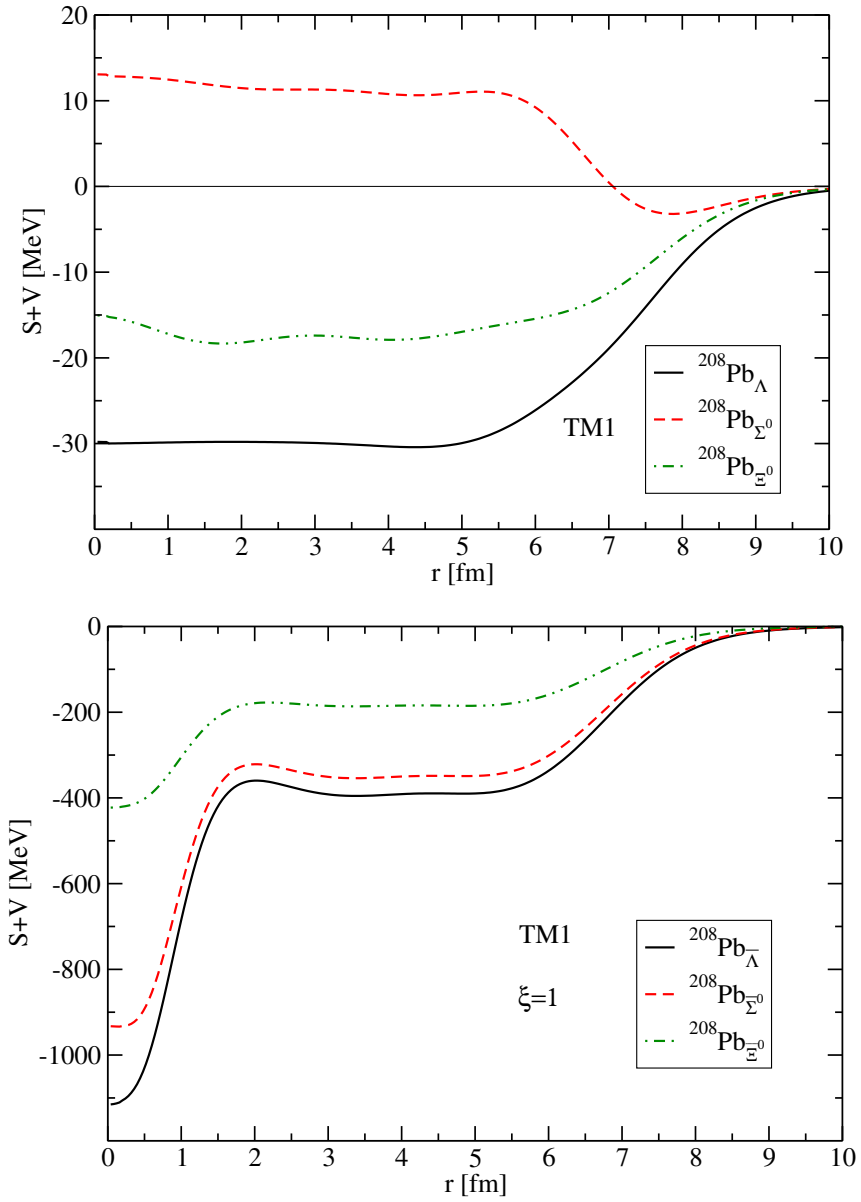

Figure 3.15: The total potential in ^{208}Pb acting on Λ, Σ^0 and Ξ^0 (top) and on $\bar{\Lambda}, \bar{\Sigma}^0$ and $\bar{\Xi}^0$ (bottom), calculated dynamically for $\xi = 1$ within the TM1 model.

The nucleon density distributions in $^{16}O_{\bar{p}}$, $^{16}O_{\bar{\Lambda}}$, $^{16}O_{\bar{\Sigma}^0}$ and $^{16}O_{\bar{\Xi}^0}$, calculated for $\xi = 1$ within the TM2 model are compared in Fig. 3.16. The corresponding densities of the antibaryons are displayed as well. The insertion of the antihyperon into the nucleus causes considerable increase of the central nucleon density. We can see the different degree of the core polarization due to the embedded antibaryon. Each antibaryon is localized up to ~ 1.5 fm in the central region of the nucleus. The densities of the $\bar{\Lambda}, \bar{\Sigma}^0$ and $\bar{\Xi}^0$ are much higher than the $\bar{p}$ density and even exceed the central density of the nuclear core. It is due to the larger mass of the antihyperons, concretely $m_{\bar{\Lambda}} = 1115$ MeV, $m_{\bar{\Sigma}^0} = 1193$ MeV and $m_{\bar{\Xi}^0} = 1315$ MeV

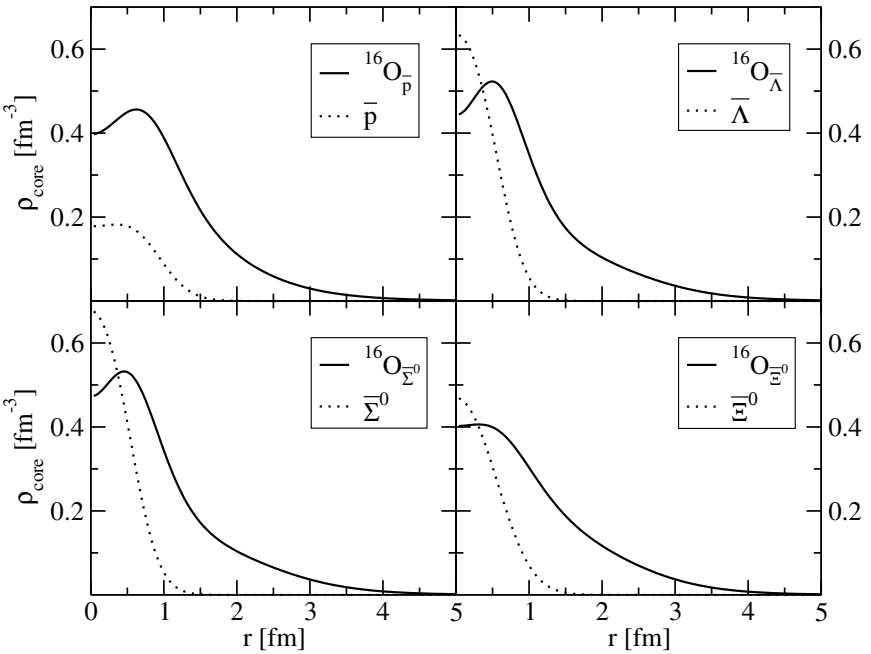

Figure 3.16: The nuclear density distribution in $^{16}O_{\bar{p}}$, $^{16}O_{\bar{\Lambda}}$, $^{16}O_{\bar{\Sigma}^0}$ and $^{16}O_{\bar{\Xi}^0}$ together with the density of the $\bar{p}, \bar{\Lambda}, \bar{\Sigma}^0$ and $\bar{\Xi}^0$, calculated for $\xi = 1$ within the TM2 model.

in comparison with the mass of the nucleon $m_N \sim 938$ MeV. Although the $\bar{\Xi}^0$ is the heaviest particle here, it does not reach the highest density since the potential it feels in the nucleus is about 400 MeV deep, in comparison with approximately 1000 MeV for $\bar{\Lambda}, \bar{\Sigma}^0$ (see Fig. 3.15), and, therefore, it is bound much less in the nucleus. The nuclear densities in $^{16}O_{\bar{\Lambda}}$ and $^{16}O_{\bar{\Sigma}^0}$ are higher than in $^{16}O_{\bar{p}}$ since there is no isovector field due to $\bar{\Lambda}$ and $\bar{\Sigma}^0$ which would affect the nucleons in the core.

In Fig. 3.17, the isovector nuclear density $\Delta\rho = \rho_p - \rho_n$ in $^{16}O_{\bar{\Lambda}}$, $^{40}Ca_{\bar{\Lambda}}$, $^{90}Zr_{\bar{\Lambda}}$ and $^{208}Pb_{\bar{\Lambda}}$ is shown. We can see that the presence of the $\bar{\Lambda}$ in the nucleus does not affect much the relative distribution of protons and neutrons in the nucleus. There is just tiny rearrangement in the central region of each nucleus ($r \leq 2.5$ fm). Being a neutral particle with zero isospin, $\bar{\Lambda}$ does not directly affect the Coulomb and isovector ρ-meson fields acting on nucleons (unlike the $\bar{p}$ in nuclei).

The isovector nuclear density $\Delta\rho$ in $^{208}Pb_{\bar{\Lambda}}$ calculated for $\xi = 1$ within the TM1 and TW99 model is displayed in Fig. 3.18. In both models, the "isovector" rearrangement of the nuclear core is small and the difference $\rho_p - \rho_n$ is negative as in the nucleus ^{208}Pb. The TW99 model predicts larger changes of $\Delta\rho$ than the TM1 model because it gives lower value of the nuclear compressibility than the TM1 model ($K = 240$ vs. $K = 281$) MeV. Therefore, the $\bar{\Lambda}$ antihyperon causes larger dynamical effects in the proton and neutron density distributions. Moreover, in the

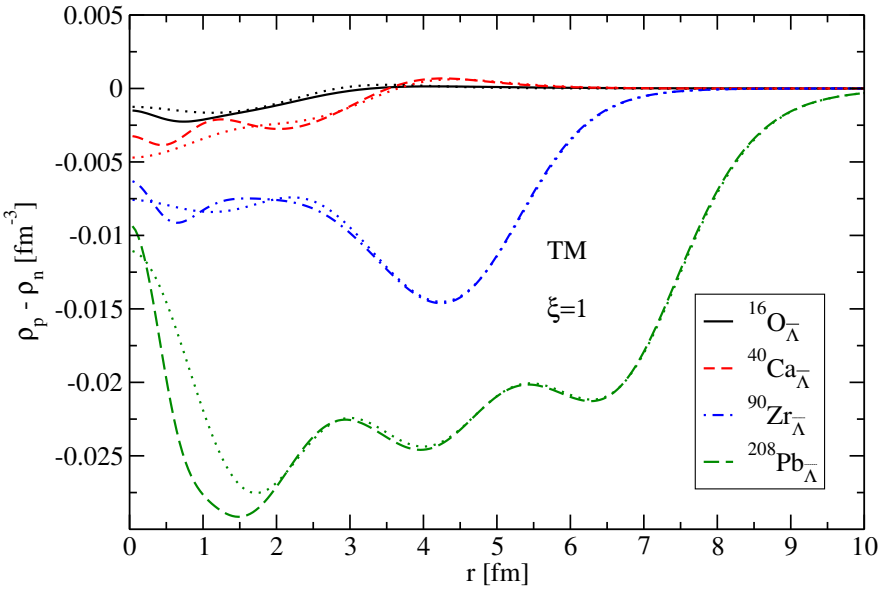

Figure 3.17: The difference between the proton and neutron density $\Delta\rho = \rho_p - \rho_n$ in selected nuclei with $\bar{\Lambda}$, calculated for $\xi = 1$ within the TM model. The difference between the proton and neutron density in normal nuclei (dotted lines) is shown for comparison.

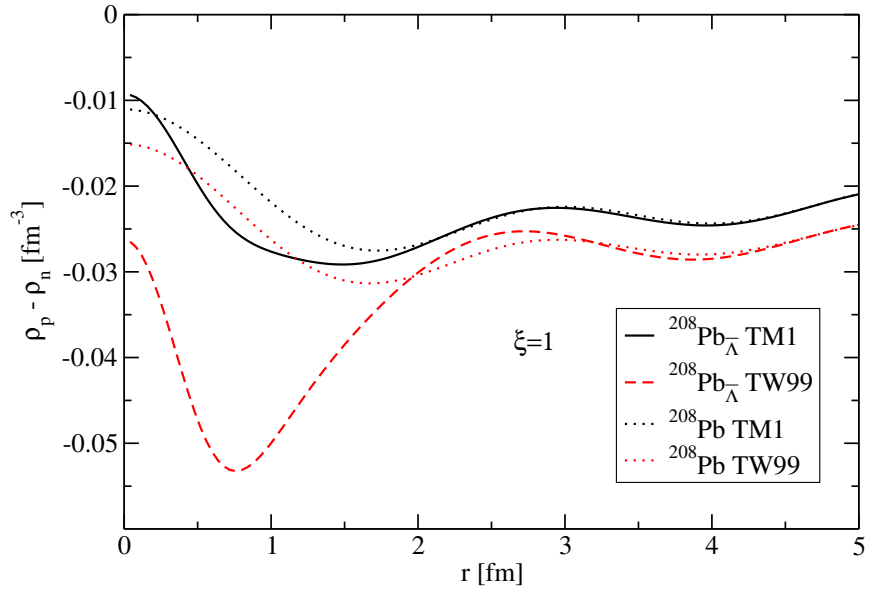

Figure 3.18: The difference between the proton and neutron density $\Delta\rho = \rho_p - \rho_n$ in $^{208}\mathrm{Pb}_{\bar{\Lambda}}$, calculated for $\xi = 1$ within the TM and TW99 model. The difference between the proton and neutron density in ^{208}Pb is shown for comparison.

TW99 model, the isovector ρ-meson field which compensates the Coulomb repulsion of protons is significantly reduced in the central region of the nucleus (see Fig. 3.9). Consequently, the difference between the proton and neutron densities increases.

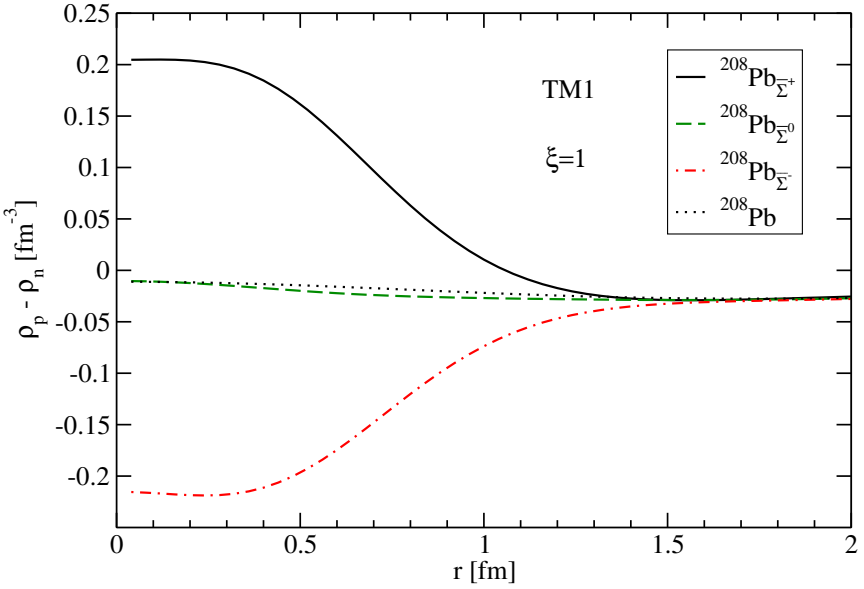

Figure 3.19: The difference between the proton and neutron density $\Delta\rho = \rho_p - \rho_n$ in $^{208}Pb_{\bar{\Sigma}^+}$, $^{208}Pb_{\bar{\Sigma}^0}$ and $^{208}Pb_{\bar{\Sigma}^-}$, calculated for $\xi = 1$ within the TM1 model. The $\Delta\rho$ in ^{208}Pb is shown for comparison.

The effect of the isovector ρ field is illustrated in Fig. 3.19, where the difference between the proton and neutron densities in $^{208}Pb_{\bar{\Sigma}^+}$, $^{208}Pb_{\bar{\Sigma}^0}$ and $^{208}Pb_{\bar{\Sigma}^-}$ is shown. Calculations were performed for $\xi = 1$ within the TM1 model. The proton density is considerably higher than the neutron density in the central region of the $^{208}Pb_{\bar{\Sigma}^+}$ nucleus. The $\bar{\Sigma}^+$ has a negative charge and the projection of isospin $T_3 = -1$, so protons feel Coulomb and isovector attraction from $\bar{\Sigma}^+$ and are thus more concentrated in the center of the nucleus than neutrons which feel isovector repulsion. The same phenomenon was observed in the $\bar{p}$ nuclei (see Fig. 3.8). In the case of $\bar{\Sigma}^-$, the situation is just opposite: protons feel the Coulomb and isovector repulsion and neutrons feel isovector attraction and, therefore, neutrons are more concentrated in the central region of $^{208}Pb_{\bar{\Sigma}^-}$. The rearrangement of the core is considerable up to ~ 1.5 fm which corresponds with the location of the $\bar{\Sigma}$ in the nucleus. In $^{208}Pb_{\bar{\Sigma}^0}$, the rearrangement of the $\rho_p - \rho_n$ density distribution is minimal since the $\bar{\Sigma}^0$ is neutral with zero isospin (it is similar to the case of $\bar{\Lambda}$ nuclei).

The nucleon single particle energies in $^{16}O_{\bar{\Sigma}^-}$, $^{16}O_{\bar{\Sigma}^0}$ and $^{16}O_{\bar{\Sigma}^+}$ calculated for $\xi = 1$ within the TM2 and TW99 model, are displayed in Fig. 3.20. The nucleons in the $1s_{1/2}$ state are very deeply bound due to the presence of the strongly interacting $\bar{\Sigma}$. The splitting between the $1s$ and $1p$ levels significantly increases due to the deeper and narrower potential well in the $\bar{\Sigma}$ nucleus. The spin-orbit splitting of the p levels also increases since the spin-orbit interaction depends on the sum of the absolute values of the vector and scalar potentials which are very deep in the $\bar{\Sigma}$

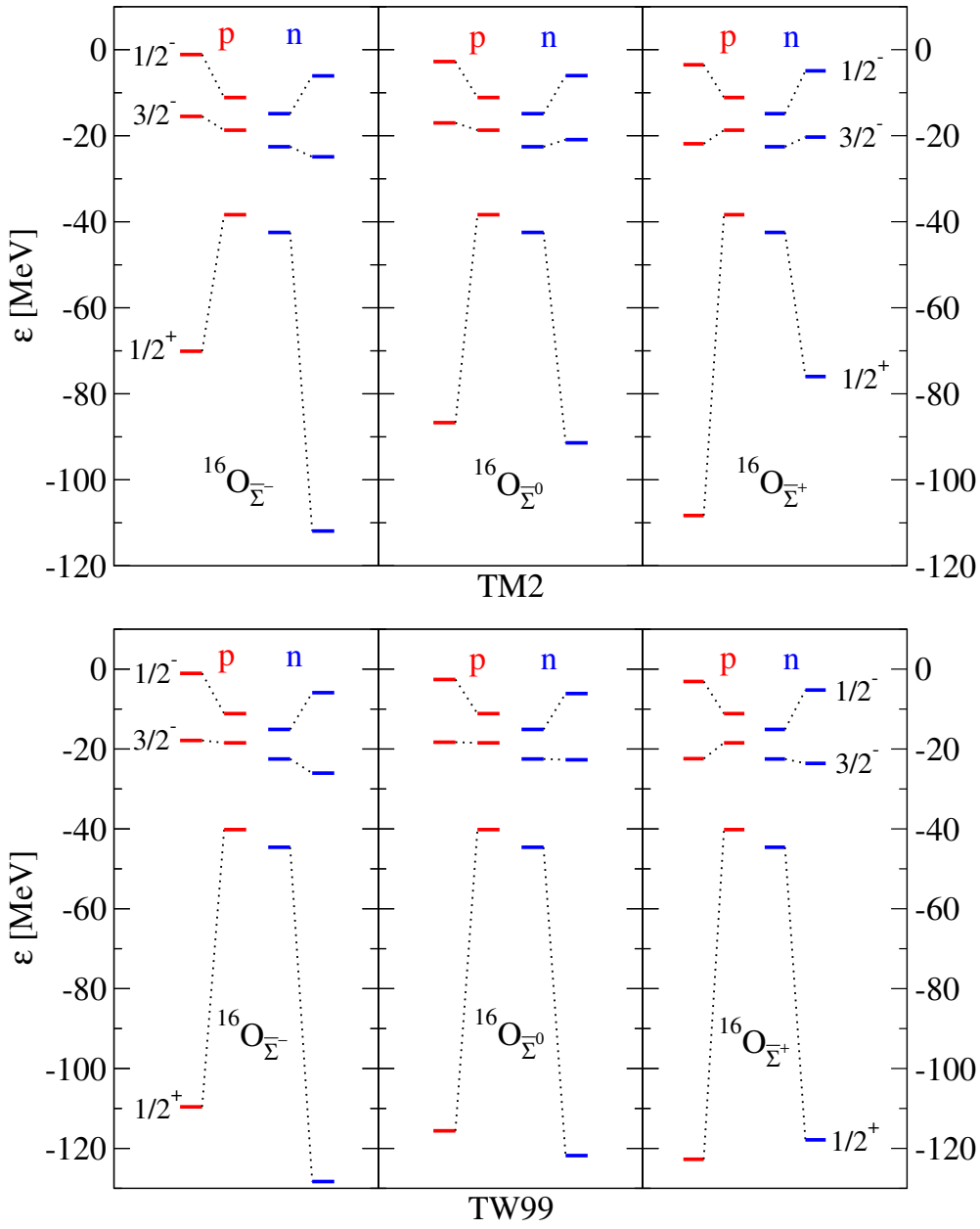

Figure 3.20: The nucleon single particle energies in $^{16}O_{\bar{\Sigma}^-}$, $^{16}O_{\bar{\Sigma}^0}$ and $^{16}O_{\bar{\Sigma}^+}$, calculated for $\xi = 1$ within the TM2 (top) and TW99 (bottom) model. The nucleon single particle energies in ^{16}O are shown in the middle of each graph.

nucleus. Due to this larger splitting, the $1p_{1/2}$ level is even less bound than in the ordinary nucleus. The same effect was observed in the $\bar{p}$ nuclei (see Fig. 3.10). The different binding of protons and neutrons in $^{16}O_{\bar{\Sigma}^-}$ and $^{16}O_{\bar{\Sigma}^+}$ is due to the isovector and Coulomb interactions which depend on the isospin projection of the $\bar{\Sigma}$. In the TW99 model, the protons and neutrons in the $1s_{1/2}$ level are more bound than in the TM2 model. It results from the lower compressibility of the TW99 model. Moreover, the repulsive ω field (and to a lesser extent also the attractive σ field)

Table 3.9: The $1s$ single particle energies $E_{\bar{B}}$ of antihyperons and the total binding energies B in ^{16}O and ^{208}Pb, calculated for $\xi = 1$ within the TM model (in MeV).

	$E_{\bar{B}}$	B		$E_{\bar{B}}$	B
$^{16}\mathrm{O}_{\bar{\Lambda}}$	-859.1	-901.4	$^{208}\mathrm{Pb}_{\bar{\Lambda}}$	-790.9	-2317.7
$^{16}\mathrm{O}_{\bar{\Sigma}^0}$	-760.8	-813.7	$^{208}\mathrm{Pb}_{\bar{\Sigma}^0}$	-698.6	-2237.2
$^{16}\mathrm{O}_{\bar{\Sigma}^-}$	-700.0	-777.9	$^{208}\mathrm{Pb}_{\bar{\Sigma}^-}$	-608.7	-2181.0
$^{16}\mathrm{O}_{\bar{\Sigma}^+}$	-711.3	-788.2	$^{208}\mathrm{Pb}_{\bar{\Sigma}^+}$	-638.1	-2214.7
$^{16}\mathrm{O}_{\bar{\Xi}^0}$	-356.4	-442.3	$^{208}\mathrm{Pb}_{\bar{\Xi}^0}$	-295.3	-1882.6
$^{16}\mathrm{O}_{\bar{\Xi}^-}$	-350.3	-437.0	$^{208}\mathrm{Pb}_{\bar{\Xi}^-}$	-283.0	-1869.7

is weaker due to the density dependence of the coupling constants in the TW99 model. The combination of the above effects causes that the nucleons are allowed to get closer to each other and, consequently, they are more bound. The smaller difference between the proton and neutron $1s_{1/2}$ single particle energies in $^{16}\mathrm{O}_{\bar{\Sigma}^-}$ and $^{16}\mathrm{O}_{\bar{\Sigma}^+}$ in the TW99 model is due to the weaker isovector ρ field in the center of the nucleus. The protons and neutrons do not feel so strong isovector attraction (repulsion) as in the TM2 model.

In Table 3.9, we present the $1s$ single particle energies $E_{\bar{B}}$ and the total binding energies in ^{16}O and ^{208}Pb, calculated for $\xi = 1$ within the TM model. The total binding energy of the nucleus with the antihyperon increases considerably when compared with the binding energy of the original ^{16}O and ^{208}Pb, $B = -128.6$ MeV and -1634.8 MeV, respectively. The antihyperon single particle energies are sizeable as well. The most tightly bound antihyperon is $\bar{\Lambda}$ while the $\bar{\Xi}$ antihyperon is bound almost 3 times less, as could be expected from inspection of the corresponding potential depths in Fig. 3.15. The differences between the $\bar{\Sigma}^0$, $\bar{\Sigma}^-$ and $\bar{\Sigma}^+$ single particle energies, as well as the total binding energies B are caused by the interplay between the Coulomb and isovector ρ-meson potentials. The same holds for $\bar{\Xi}^0$ and $\bar{\Xi}^-$.

Chapter 4

Conclusion

In this work, antibaryon–nucleus bound states were calculated with the aim to study dynamical effects caused by the presence of a strongly interacting antibaryon in a nucleus. We added $\bar{p}$, $\bar{\Lambda}$, $\bar{\Sigma}$ and $\bar{\Xi}$ into the $1s_{1/2}$ state of selected nuclei across the periodic table and performed self-consistent calculations within the RMF model. We used different parametrizations of the RMF model; here we presented results for the nonlinear TM1 and TM2 models, and the density–dependent TW99 model. The antibaryon–nucleus interactions were constructed by the G-parity transformation of the baryon–meson coupling constants. Possible deviations of the couplings from the G-parity values were taken into account by introducing a scaling factor. Dynamical and static calculations were performed in order to illustrate the core polarization effects due to the strongly interacting antibaryon. We focused on nuclear density distributions, nuclear binding energies and antibaryon potentials, densities and single particle energies.

A substantial part of this work was devoted to the antiproton–nucleus interaction. Theoretical understanding of this interaction is needed for future experiments with antiprotons at FAIR [39]. We revealed that the insertion of the antiproton into the nucleus causes remarkable changes in the nuclear structure. The $\bar{p}$ potential becomes strongly attractive due to the G-parity transformation and, vice versa, nucleons in a nucleus feel strong attraction from the $\bar{p}$. The depth of the antiproton potential reaches nearly 1700 MeV in both parameter sets, which results in the deeply bound $\bar{p}$ in the nucleus. However, the large increase of the $\bar{p}$ potential is restricted to the very center of the nucleus ($r \leq 2$ fm) where the antiproton is localized. We found strong polarization effects in the $\bar{p}$ nuclei. The central nuclear density considerably increases—it reaches about 3 times the normal nuclear density. The nucleus $^{16}\mathrm{O}_{\bar{p}}$ is affected as a whole by the presence of the antiproton, while in the case of heavier nuclei such as ^{40}Ca, ^{90}Zr and ^{208}Pb, the polarization effects are significant only in the small central region of these nuclei and the rest of their vol-

ume remains unchanged. These effects were observed in the both considered RMF models.

The nucleon single particle energies in a nucleus are also affected by the deeply bound antiproton—in particular, the $1s_{1/2}$ and $2s_{1/2}$ proton and neutron single particle energies become considerable. The spin-orbit splitting in $\bar{p}$ nuclei is larger and also the spacing between the $1s$ and $1p$ levels increases due to the deep and narrower potential well. Huge dynamical changes in $\bar{p}$ nuclei result in extremely large binding energies, as well as binding energies per particle.

The antiproton in a nucleus feels an "attractive", as well as "repulsive" self-interaction which leads to the saturation of the $\bar{p}$ density distribution and subsequently to its decrease. The effects of self-interaction starts to be pronounced for larger values of scaling parameter ξ. For the values of $\xi \sim 0.2 - 0.3$, which seem to yield a realistic $\bar{p}$–nucleus interaction, the effect is tiny and thus can be neglected.

We considered the absorption of $\bar{p}$ in a nucleus. We adopted the imaginary part of a phenomenological optical potential in our calculations to account for the annihilation. Its parameters were constrained by fits to $\bar{p}$-atomic data. We considered $\bar{N}N$ annihilation at rest to various decay channels and took into account the phase space suppression for the annihilation products due to the deeply bound $\bar{p}$ in the nuclear medium. The $\bar{p}$ widths significantly decrease when the suppression of the phase space is considered, however, they still remain sizeable for a realistic $\bar{p}$–nucleus interaction. We noticed that the $\bar{p}$ absorption remarkably influenced the polarization of a nucleus. Therefore, it is important to perform the calculations with the complex $\bar{p}$–nucleus potential fully self-consistently. Such calculations were performed in this work for the first time ever.

We also performed first calculations of the nuclear bound states of various antihyperons. Even though the Λ, Σ^0 and Ξ^0 hyperons are bound weakly in the nucleus or are not bound at all, the corresponding antihyperons are deeply bound in a nucleus due to the G-parity transformation. The $\bar{\Lambda}$ and $\bar{\Sigma}$ potential is about 1000 MeV deep and the $\bar{\Xi}$ potential reaches about 400 MeV. We observed similar polarization effects in the nuclear core as in the case of the antiproton. We studied the role of the isovector field ρ in nuclei with a bound antihyperon in both RMF models. The nucleon single particle energies are significantly affected by the presence of the antihyperon and the total binding energies increase as well. We found similar behavior of the single particle energies as in the $\bar{p}$ nuclei.

In further studies, it would be necessary to incorporate the absorption of antihyperons in the nuclear medium and perform self-consistent calculations for the complex antihyperon–nucleus potentials. Moreover, it would be desirable to consider the energy dependence of the $\bar{p}$–nucleus interaction, which would allow to

describe not only $\bar{p}$–nucleus bound states but also scattering processes. The study of a possible formation of antibaryonic nuclear bound states, as well as post annihilation dynamics of the nucleus is expected to be in great demand in view of future experiments at FAIR [39].

Appendix A

Notation and conventions

We adhere to the convention of Serot and Walecka [18]. Natural physical units are chosen with $\hbar = c = 1$. Contravariant x_μ and covariant x^μ four vectors are written as

$$x \equiv x^\mu = (t, \vec{x}), \quad x_\mu = (t, -\vec{x}) \ , \tag{A.1}$$

$$\partial^\mu \equiv \frac{\partial}{\partial x_\mu} = \left(\frac{\partial}{\partial t}, -\vec{\nabla}\right), \quad \partial_\mu \equiv \frac{\partial}{\partial x^\mu} = \left(\frac{\partial}{\partial t}, \vec{\nabla}\right) \ . \tag{A.2}$$

The Dirac equation for a free particle of mass M reads

$$(i\gamma_\mu \partial^\mu - M)\psi = (i\not{\partial} - M)\psi = 0 \ , \tag{A.3}$$

where we use the Feynman "slash" notation $\not{a} = a_\mu \gamma^\mu$. The gamma matrices $\gamma^\mu = (\gamma^0, \vec{\gamma})$ obey

$$\gamma^\mu \gamma^\nu + \gamma^\nu \gamma^\mu = \{\gamma^\mu, \gamma^\nu\} = 2g^{\mu\nu}, \tag{A.4}$$

where $g^{\mu\nu}$ is a metric tensor given by

$$g^{\mu\nu} = \begin{pmatrix} 1 & 0 & 0 & 0 \\ 0 & -1 & 0 & 0 \\ 0 & 0 & -1 & 0 \\ 0 & 0 & 0 & -1 \end{pmatrix}, \tag{A.5}$$

and in the standard (Dirac-Pauli) realization are given as

$$\beta = \gamma^0 = \begin{pmatrix} \mathbb{1} & 0 \\ 0 & -\mathbb{1} \end{pmatrix}, \quad \vec{\alpha} = \begin{pmatrix} 0 & \vec{\sigma} \\ \vec{\sigma} & 0 \end{pmatrix}, \quad \vec{\gamma} = \beta\vec{\alpha} = \begin{pmatrix} 0 & \vec{\sigma} \\ -\vec{\sigma} & 0 \end{pmatrix}, \tag{A.6}$$

with Pauli matrices defined by

$$\sigma_1 = \begin{pmatrix} 0 & 1 \\ 1 & 0 \end{pmatrix}, \quad \sigma_2 = \begin{pmatrix} 0 & -i \\ i & 0 \end{pmatrix}, \quad \sigma_3 = \begin{pmatrix} 1 & 0 \\ 0 & -1 \end{pmatrix}. \tag{A.7}$$

The nucleon wave functions are considered as isospin doublets, i. e.

$$\psi_i = \begin{pmatrix} \psi_p \\ \psi_n \end{pmatrix}, \tag{A.8}$$

where ψ_p and ψ_n denotes proton and neutron wave functions, respectively.

Appendix B

Numerical solution of the equations of motion

We seek for a static solution of Dirac equation (2.10) in the form

$$\psi(x^\mu) = e^{-i\epsilon t}\psi(\vec{x}) \ . \tag{B.1}$$

Then we have

$$\mathcal{H}\psi(\vec{x}) = E\psi(\vec{x}) \ , \tag{B.2}$$

where

$$\mathcal{H} = [-i\vec{\alpha}\vec{\nabla} + \beta(m_N + g_{\sigma j}\sigma) + g_{\omega j}\omega_0 + g_{\rho j}\rho_0\tau_3 + e_j\frac{(1+\tau_3)}{2}A_0] \ . \tag{B.3}$$

is the single-particle Dirac Hamiltonian. The field $\psi(\vec{x})$ can be expanded using positive $u_\beta(\vec{x})$ and negative $v_\beta(\vec{x})$ energy solutions as

$$\psi(\vec{x}) = \sum_\beta \hat{a}_\beta u_\beta(\vec{x}) + \hat{b}^\dagger_\beta v_\beta(\vec{x}) \tag{B.4}$$

in the Schrödinger picture. The operators $\hat{a}_\beta$ and $\hat{b}^\dagger_\beta$ are the annihilation and creation operators for baryons and antibaryons, respectively. They fulfill the well-known anticommutation relations for fermions. The index β involves the full set of quantum numbers describing the single-particle solution. Since the system is assumed spherically symmetric and parity conserving, β contains the usual angular momentum and parity quantum numbers. The Dirac Hamiltonian (B.3) is linear in $\vec{p}$ and so it does not commute with angular momentum $\vec{L}$. It also does not commute with spin operator $\vec{S} = \frac{\vec{\Sigma}}{2}$. But, if we define single-particle angular momentum operator as

$$\vec{J} = \vec{L} + \vec{S} \ , \tag{B.5}$$

it is easy to show that (B.3) is rotationally invariant, i. e.

$$[\mathcal{H}, J_i] = [\mathcal{H}, \vec{J}^2] = 0 \quad \text{for} \quad i = 1, 2, 3 \ . \tag{B.6}$$

Thus the quantum numbers j and m of angular momentum may be used to label the states. Since Hamiltonian (B.3) obeys $[\mathcal{H}, \vec{S}^2] = 0$, the spin $s = 1/2$ is a constant of the motion. Moreover, by defining the operator

$$\mathcal{K} = \gamma^0[\vec{\Sigma}.\vec{J} - 1/2] = \gamma^0[\vec{\Sigma}.\vec{L} + 1] \ , \tag{B.7}$$

it is straightforward to show that $[\mathcal{H}, \mathcal{K}] = 0$, which provides another constant of motion. This is a consequence of parity conservation. The eigenvalues of the operator $\mathcal{K}$ are

$$-\kappa = \pm(j + 1/2) \ , \tag{B.8}$$

where κ is a non-zero integer, since

$$\mathcal{K}^2 = \vec{L}^2 + \vec{\Sigma}.\vec{L} + 1 = \vec{J}^2 + 1/4 \ . \tag{B.9}$$

If we define the upper and lower component of the wave function by

$$\psi = \begin{pmatrix} \psi_A \\ \psi_B \end{pmatrix} \tag{B.10}$$

and act on this wave function with $\mathcal{K}$:

$$\mathcal{K}\psi = -\kappa\psi = \begin{pmatrix} -\kappa\psi_A \\ -\kappa\psi_B \end{pmatrix} = \begin{pmatrix} (\vec{\sigma}.\vec{L} + 1)\psi_A \\ -(\vec{\sigma}.\vec{L} + 1)\psi_B \end{pmatrix} \ , \tag{B.11}$$

we find that ψ_A and ψ_B are eigenstates of $(\vec{\sigma}.\vec{L}+1)$ with opposite eigenvalues. Since $\vec{L}^2 = \vec{J}^2 - \vec{\sigma}.\vec{L} - 3/4$, it holds that

$$\vec{L}^2\psi_A = [(j + 1/2)^2 + \kappa]\psi_A \equiv l_A(l_A + 1)\psi_A \ , \tag{B.12}$$

$$\vec{L}^2\psi_B = [(j + 1/2)^2 - \kappa]\psi_B \equiv l_B(l_B + 1)\psi_B \ . \tag{B.13}$$

This implies that upper and lower components are separately eigenstates of $\vec{L}^2$, although ψ is not. For given values of j and κ, the value of l may be determined

from

$$j(j+1) - l_A(l_A+1) + 1/4 = -\kappa \ , \tag{B.14}$$

$$j(j+1) - l_B(l_B+1) + 1/4 = \kappa \ . \tag{B.15}$$

The two-component wave functions have fixed j and $s = 1/2$, therefore, l_A and l_B must be $j \pm 1/2$. Their angular momentum and spin parts are

$$\begin{aligned} \Phi_{\kappa m} &= \sum_{m_l m_s} \langle l m_l s m_s | j m \rangle \, Y_{l m_l}(\theta, \phi) \chi_{m_s} \ , \\ j = |\kappa| - 1/2, \qquad l &= \begin{cases} \kappa & \kappa > 0 \\ -(\kappa+1) & \kappa < 0 \ , \end{cases} \end{aligned} \tag{B.16}$$

where Y_{lm_l} is a spherical harmonic and χ_{m_s} is a two-component Pauli spinor. Thus, the single-particle wave function in a central, parity conserving field may be written as

$$\psi_j^\alpha(\vec{x}) = \psi_j^{n\kappa m t}(\vec{x}) = \begin{pmatrix} i[G_j^{n\kappa t}(r)/r]\Phi_{\kappa m} \\ -[F_j^{n\kappa t}(r)/r]\Phi_{-\kappa m} \end{pmatrix} \zeta_t \ , \tag{B.17}$$

where ζ_t is a two-component isospinor and G_j^α and F_j^α is the large and small component of the Dirac spinor ($j = N, \bar{B}$), respectively. Because Hamiltonian (B.3) commutes with the isospin operators T_3 and T^2, the states may be labeled by their charge or isospin projection t ($t = 1/2$ for protons and $t = -1/2$ for neutrons). The principal quantum number is denoted by n. The phase choice in (B.17) leads to real bound-state wave-functions G_j^α and F_j^α for real potentials in (B.2).

Once we have a general form of the solution in (B.17), we may now evaluate the local meson source terms in the meson field equations. We assume that the nuclear ground state consists of filled shells up to some value of n and κ. This is consistent with spherical symmetry and is appropriate for doubly magic nuclei. We also assume that all bilinear products of baryon operators are normal ordered. With these assumptions, the local baryon density becomes

$$\begin{aligned} \rho_N(\vec{x}) &= \langle \underline{F} | : \hat{\psi}^\dagger(\vec{x}) \hat{\psi}(\vec{x}) : | \underline{F} \rangle \\ &= \sum_\beta u_\beta^\dagger(\vec{x}) u_\beta(\vec{x}) \\ &= \sum_\alpha \left(\frac{2j_\alpha + 1}{4\pi r^2} \right) (|G_N^\alpha(r)|^2 + |F_N^\alpha(r)|^2) \ , \end{aligned} \tag{B.18}$$

where $|\underline{F}\rangle$ is the filled-shell ground state and the colons imply that $\psi^\dagger\psi$ is normal

ordered. With these results, we can rewrite the meson field equations (2.11) as

$$\begin{aligned}\left(\frac{d^2}{dr^2}+\frac{2}{r}\frac{d}{dr}-m_\sigma^2\right)\sigma(r) =& g_{\sigma N}\rho_S + g_2\sigma + g_3\sigma^2 + g_{\sigma\bar{B}}\rho_{S\bar{B}} \\ =& g_{\sigma N}\sum_\alpha\left(\frac{2j_\alpha+1}{4\pi r^2}\right)(|G_N^\alpha(r)|^2-|F_N^\alpha(r)|^2) \\ &+ g_{\sigma\bar{B}}\left(\frac{1}{4\pi r^2}\right)(|G_{\bar{B}}(r)|^2-|F_{\bar{B}}(r)|^2) \\ &+ g_2\sigma + g_3\sigma^2\ , \end{aligned} \tag{B.19}$$

$$\begin{aligned}\left(\frac{d^2}{dr^2}+\frac{2}{r}\frac{d}{dr}-m_{\omega_0}^2\right)\omega_0(r) =& -g_{\omega N}\rho_V + g_{\omega\bar{B}}\rho_{V\bar{B}} + d\omega_0^3 \\ =& -g_{\omega N}\sum_\alpha\left(\frac{2j_\alpha+1}{4\pi r^2}\right)(|G_N^\alpha(r)|^2+|F_N^\alpha(r)|^2) \\ &+ g_{\omega\bar{B}}\left(\frac{1}{4\pi r^2}\right)(|G_{\bar{B}}(r)|^2+|F_{\bar{B}}(r)|^2) \\ &+ d\omega_0^3\ , \end{aligned} \tag{B.20}$$

$$\begin{aligned}\left(\frac{d^2}{dr^2}+\frac{2}{r}\frac{d}{dr}-m_\rho^2\right)\rho_0(r) =& -g_{\rho N}\rho_I - g_{\rho\bar{B}}\rho_{I\bar{B}} \\ =& -g_{\rho N}\sum_\alpha\left(\frac{2j_\alpha+1}{4\pi r^2}\right)t_\alpha(|G_N^\alpha(r)|^2+|F_N^\alpha(r)|^2) \\ &- g_{\rho\bar{B}}\left(\frac{1}{4\pi r^2}\right)t_{\bar{B}}(|G_{\bar{p}}(r)|^2+|F_{\bar{p}}(r)|^2)\ , \end{aligned} \tag{B.21}$$

$$\begin{aligned}\left(\frac{d^2}{dr^2}+\frac{2}{r}\frac{d}{dr}\right)A_0(r) =& -e\rho_p + e_{\bar{B}}\rho_{\bar{B}} \\ =& -e\sum_\alpha\left(\frac{2j_\alpha+1}{4\pi r^2}\right)\frac{(t_\alpha+1)}{2}(|G_N^\alpha(r)|^2-|F_N^\alpha(r)|^2) \\ &+ e_{\bar{B}}\left(\frac{1}{4\pi r^2}\right)\frac{(t_{\bar{B}}+1)}{2}(|G_{\bar{B}}(r)|^2+|F_{\bar{B}}(r)|^2)\ . \end{aligned} \tag{B.22}$$

The equations for the (anti)baryon wave functions are obtained by substituting

(B.17) into (B.2)

$$\frac{d}{dr}G_j^\alpha(r) + \frac{\kappa}{r}G_j^\alpha(r) - [\epsilon_j^\alpha - g_{\omega j}\omega_0 - t_a g_{\rho j}\rho_0(r) - (t_\alpha + 1/2)e_j A_0(r) + m_j - g_\sigma \sigma(r)]F_j^\alpha(r) = 0 \ , \tag{B.23}$$

$$\frac{d}{dr}F_j^\alpha(r) - \frac{\kappa}{r}F_j^\alpha(r) + [\epsilon_j^\alpha - g_{\omega j}\omega_0(r) - t_a g_{\rho j}\rho_0(r) - (t_\alpha + 1/2)e_j A_0(r) - m_j + g_{\sigma j}\sigma(r)]G_j^\alpha(r) = 0 \ . \tag{B.24}$$

The normalization condition that yields unit probability for finding each particle somewhere in space is

$$\int_0^\infty dr(|G_j^\alpha(r)|^2 + |F_j^\alpha(r)|^2) = 1 \ . \tag{B.25}$$

The equations (B.19) - (B.24) are coupled nonlinear differential equations that can be solved by an iterative procedure. For a given set of meson fields, the Dirac equations (B.23) and (B.24) are solved by the Runge-Kutta method integrating outward from the origin and inward from large r, matching the solutions at some intermediate radius to determine the eigenvalues E_j^α. Analytic solutions in the regions of a small and large r allow the proper boundary conditions to be imposed. Once the baryon wave functions are determined, the source terms may be evaluated and the meson fields calculated by integrating over the static Green's function

$$D(r, r'; m_i) = \frac{-1}{m_i r r'} \sinh(m_i r_<) \exp(-m_i r_>) \ . \tag{B.26}$$

This Green's function embodies the boundary conditions for exponential decay at large r and vanishing slope for the fields at origin. For example, the solution of eq. (B.19) for the scalar field reads

$$\sigma(r) = \int_0^\infty r'^2 dr'[-g_{\sigma N}\rho_S(r')]D(r, r'; m_\sigma) \ . \tag{B.27}$$

The new meson fields are used to compute the potentials entering the Dirac equations. The solution of the Dirac equations yields spinors for the next iteration. This procedure is repeated until the self-consistency is reached.

The total energy of the system can be expressed as

$$
\begin{aligned}
E = \langle \underline{F}|\mathcal{H}|\underline{F}\rangle = \int d^3x \{ & \frac{1}{2}[(\nabla\sigma)^2 + m_\sigma^2\sigma^2] - \frac{1}{2}[(\nabla\omega_0)^2 + m_\omega^2 + \omega_0^2] \\
& - \frac{1}{2}(\nabla A_0)^2 - \frac{1}{2}[(\nabla\rho_0)^2 + m_\rho^2\rho_0^2] + \langle \underline{F}| : \psi^\dagger[-i\vec{\alpha}.\vec{\nabla} + \beta(m_N + g_{\sigma j}\sigma) \\
& + g_{\omega j}\omega_0 + g_{\rho j}\rho_0\tau_3 + e_j\frac{1+\tau_3}{2}A_0]\psi : |\underline{F}\rangle\} \ .
\end{aligned}
\tag{B.28}
$$

The part involving baryon fields can be evaluated using the Dirac equation (B.3)

$$
\int d^3x \sum_\alpha \epsilon_j^\alpha \left(\frac{2j+1}{4\pi r^2}\right)(|G_j^\alpha(r)|^2 + |F_j^\alpha(r)|^2) = \sum_\alpha \epsilon_j^\alpha \ . \tag{B.29}
$$

For the meson terms, the exponential decay of the fields at large r permits the following partial integration:

$$
\begin{aligned}
\int d^3x \frac{1}{2}[(\nabla\sigma)^2 + m_\sigma^2\sigma^2] &= \frac{1}{2}\int d^3x[\sigma(-\nabla^2 + m_\sigma^2)\sigma] \\
&= \frac{1}{2}\int d^3x g_\sigma \rho_S(r)\sigma(r) \ ,
\end{aligned}
\tag{B.30}
$$

where the final equality follows from the equation (B.19). Similarly, we can rewrite the other terms and therefore we can express the energy as

$$
\begin{aligned}
E = & \sum_\alpha \epsilon_j^\alpha + \epsilon_{\bar{B}}^\alpha \\
& - \frac{1}{2}\int \mathrm{d}^3x \ (-g_{\sigma N}\,\sigma\rho_S + g_{\omega N}\,\omega_0\rho_V + g_{\rho N}\,\rho_0\rho_I + e\,A_0\rho_p) \\
& - \frac{1}{2}\int \mathrm{d}^3x \ (-\tfrac{1}{3}g_2\,\sigma^3 - \tfrac{1}{2}g_3\,\sigma^4 + \tfrac{1}{2}d\,\omega^4) \\
& - \frac{1}{2}\int \mathrm{d}^3x \ (-g_{\sigma\bar{B}}\,\sigma\rho_{S\bar{B}} + g_{\omega\bar{B}}\,\omega_0\rho_{V\bar{B}} + g_{\rho\bar{B}}\,\rho_0\rho_{I\bar{p}} - e_{\bar{B}}\,A_0\rho_{\bar{B}}) \ .
\end{aligned}
\tag{B.31}
$$

Bibliography

[1] T.J. Bürvenich, W. Greiner, I.N. Mischustin, L.M. Satarov, H. Stöcker, Phys. Rev. **C 71** (2005) 035201.

[2] A.B. Larionov, I.N. Mischustin, L.M Satarov, W. Greiner, Phys. Rev. **C 78** (2008) 014604.

[3] A.B. Larionov, I.N. Mischustin, I.A. Pschenichnov, L.M. Satarov, W. Greiner, Acta Phys.Polon. **B 41** (2010) 299.

[4] T. Bürvenich, I.N. Mischustin, L.M. Satarov, J.A. Maruhn, H. Stöcker, W. Greiner, Phys.Lett. **B 542** (2002) 261.

[5] T. Gaitanos, M. Kaskulov, H. Lenske, Phys. Lett. **B 703** (2011) 193.

[6] The PANDA experiment [online]
URL:<http://www-panda.gsi.de/> [cit. 30.4.2013]

[7] O. Chamberlaine *et al.*, Phys. Rev. **100** (1955) 947.

[8] R. Armenteros, B. French, *High-Energy Physics*. Vol. **4**, (Academic Press New York 1969).

[9] T. Walcher, Ann. Rev. Nucl. Part. Sci. **38** (1988) 67.

[10] G.E. Walker, Ch.D. Goodman and C. Olmer (Eds.), *Antinucleon– and Nucleon–Nucleus Interaction*, (Plenum Press 1985).

[11] C. Amsler, Rev. Mod. Phys. **70** (1998) 1293.

[12] E. Klempt, C. Batty, J.-M. Richard, Phys. Rep. **413** (2005) 197

[13] C.J. Batty, E. Friedman, A. Gal, Phys. Rep. **287** (1997) 385.

[14] E. Friedman, A. Gal, Phys. Rep. **452** (2007) 89.

[15] E. Friedman, A. Gal, J. Mareš, Nucl. Phys. **A 761** (2005) 283.

[16] L. Tauscher, *Antiproton–nucleon and antiproton–nucleus bound states*, Proc. 8th European Symposium on Nucleon-antinucleon Interactions, Thessaloniki, 1–5 Sep 1986, pp.247-257.

[17] R. Machleidt, Adv. Nucl. Phys. **19** (1988) 189.

[18] B.D. Serot, J.D. Walecka, Adv. Nucl. Phys. **16** (1986) 1.

[19] P.-G. Reinhardt, Rep. Prog. Phys. **52** (1989) 439.

[20] B.D. Serot, J.D. Walecka, Int. J. Mod. Phys. **E 6** (1996) 515.

[21] The GiBUU model [online]
URL:<http://gibuu.physik.uni-giessen.de/GiBUU> [cit. 30.4.2013]

[22] A. Gal, R.S. Hayano (Eds.), *Recent Advances in Strangeness Nuclear Physics*, Nucl. Phys. **A 804** (2008) 171.

[23] B.F. Gibson, K. Imai, T. Motoba, T. Nagae, A. Ohnishi (Eds.), Proc. 10th Int. Conf. on Hypernuclear nad Strange Paticle Physics, Tokai, 14–18 September 2009, Nucl. Phys. **A 835** (2010) 1.

[24] P. Bydžovský, A. Gal, J. Mareš (Eds.), *Topics in Strangeness Nuclear Physics*, Lect. Notes Phys. **724** (2007) 1.

[25] J. Pochodzalla, Phys. Lett. **B 669** (2008) 306.

[26] S. Typel, H.H. Wolter, Nucl. Phys. **A 656** (1999) 331.

[27] D. Griffiths, *Introduction to elementary particles*, (John Wiley & Sons, Inc. 1987).

[28] J. Mareš, B.K. Jennings, Phys. Rev. **C 49** (1994) 2472.

[29] B.K. Jennings, Phys. Lett. **B 246** (1990) 325.

[30] J. Schaffner, C.B. Dover, A. Gal, C. Greiner, D.J. Millener and H. Stöcker, Ann. Phys. **235** (1994) 35.

[31] J. Mareš, E. Friedman, A. Gal, B.K. Jennings, Nucl. Phys. **A 594** (1995) 311.

[32] P. Khaustov *et al.*, Phys. Rev. **61** (2000) 054603.

[33] D. Gazda, E. Friedman, A. Gal and J. Mareš, Phys. Rev. **C 80** (2009) 035205.

[34] C.J. Horowitz, B.D. Serot, Nucl. Phys. **A 368** (1981) 503.

[35] P.-G. Rheihard *et al.*, Z. Phys. **A 323** (1986) 13.

[36] M.M. Sharma, M.A. Nagarajan, P. Ring, Phys. Lett. **B 312** (1993) 377.

[37] Y. Sugahara, H. Toki, Nucl. Phys. **A 579** (1994) 557.

[38] W. Long, J. Meng, N. Van Giai, S. Zhou, Phys. Rev. **C 69** (2004) 034319.

[39] The FAIR facility [online]
URL:<http://www.fair-center.eu/index.php?id=1> [cit. 3.5.2013]